remote sensing

MDPI

Article

Measuring Annual Sedimentation through High Accuracy UAV-Photogrammetry Data and Comparison with RUSLE and PESERA Erosion Models

Simoni Alexiou [1], Nikolaos Efthimiou [2], Mina Karamesouti [3,4], Ioannis Papanikolaou [1,*], Emmanouil Psomiadis [1] and Nikos Charizopoulos [1]

[1] Laboratory of Mineralogy and Geology, Department of Natural Resources & Agricultural Engineering, Agricultural University of Athens, 75 Iera Odos Str., 11855 Athens, Greece
[2] Faculty of Environmental Sciences, Czech University of Life Sciences Prague, 16500 Prague, Czech Republic
[3] Geoinformation Science Lab, Geography Department, Humboldt-Universität zu Berlin, 10117 Berlin, Germany
[4] IRI THESys, Humboldt-Universität zu Berlin, 10117 Berlin, Germany
* Correspondence: i.pap@aua.gr

Abstract: Model-based soil erosion studies have increased in number, given the availability of geodata and the recent technological advances. However, their accuracy remains rather questionable since the scarcity of field records hinders the validation of simulated values. In this context, this study aims to present a method for measuring sediment deposition at a typical Mediterranean catchment (870 ha) in Greece through high spatial resolution field measurements acquired by an Unmanned Aerial Vehicle (UAV) survey. Three-dimensional modeling is considered to be an emerging technique for surface change detection. The UAV-derived point cloud comparison, applying the Structure-from-Motion (SfM) technique at the Platana sediment retention dam test site, quantified annual topsoil change in cm-scale accuracy (0.02–0.03 m), delivering mean sediment yield of 1620 $m^3 \pm 180$ m^3 or 6.05 t $ha^{-1}yr^{-1}$ and 3500 $m^3 \pm 194$ m^3 or 13 t $ha^{-1}yr^{-1}$ for the 2020–2021 and 2021–2022 estimation. Moreover, the widely applied PESERA and RUSLE models estimated the 2020–2021 mean sediment yield at 1.12 t $ha^{-1}yr^{-1}$ and 3.51 t $ha^{-1}yr^{-1}$, respectively, while an increase was evident during the 2021–2022 simulation (2.49 t $ha^{-1}yr^{-1}$ and 3.56 t $ha^{-1}yr^{-1}$, respectively). Both applications appear to underestimate the net soil loss rate, with RUSLE being closer to the measured results. The difference is mostly attributed to the model's limitation to simulate gully erosion or to a C-factor misinterpretation. To the authors' better knowledge, this study is among the few UAV applications employed to acquire high-accuracy soil loss measurements. The results proved extremely useful in our attempt to measure sediment yield at the cm scale through UAV-SfM and decipher the regional soil erosion and sediment transport pattern, also offering a direct assessment of the retention dams' life expectancy.

Keywords: soil erosion; RUSLE; PESERA; UAV; point cloud; Structure-from-Motion; geoenvironment

Citation: Alexiou, S.; Efthimiou, N.; Karamesouti, M.; Papanikolaou, I.; Psomiadis, E.; Charizopoulos, N. Measuring Annual Sedimentation through High Accuracy UAV-Photogrammetry Data and Comparison with RUSLE and PESERA Erosion Models. *Remote Sens.* **2023**, *15*, 1339. https://doi.org/10.3390/rs15051339

Academic Editor: Emilio Rodriguez Caballero

Received: 27 January 2023
Revised: 22 February 2023
Accepted: 23 February 2023
Published: 27 February 2023

1. Introduction

Soil erosion, as a natural soil degradation process, primarily caused by the physical impact of water and wind on the exposed soil surfaces, is one of the principal factors of soil degradation [1]. The quantification of soil erosion is critical for designing and implementing appropriate river/watershed management and pollution control strategies [2]. However, the complex non-linear processes that characterize the phenomenon's evolution in space and time, i.e., sediment production, transport, and deposition [3], make the validation of modelled soil loss an intractable problem. The scientific community attempts to simulate the water-driven soil displacement by developing conceptually diverse models (i.e., process-based, agent-based, logic-based, empirical, etc.), able to perform in various spatial and

temporal scales [4–6]. In the attempt to parameterize erosion's spatiotemporal dynamics, models of different philosophies have been developed [5], e.g., process-based, empirical, conceptual, etc., such as the USLE [7], EPM [8], ANSWERS [4], RUSLE [9,10], WEPP [11], SWAT [12], PESERA [13,14], G2 [15], etc. The development of so many erosion models and their constant upgrade/modification confirm the complexity of the process and the difficulty in assessing soil erosion. As to the focal point of this research, RUSLE has been widely used in various temporal and spatial scales [16,17], while PESERA has mainly been applied at the regional level [16,18]. Both models have been employed for sheet, rill, and inter-rill erosion analysis [19,20], with RUSLE being characterized by simplicity, ease of use, and low computational demands, contrary to PESERA, which requires a vast amount of input layers [18]. The latter model was initially developed for average annual water erosion assessment in agricultural areas. It is a physical-based model, suitable for large watersheds and regional scales [21]. Sediment yield is calculated from runoff and each storm event, resulting in the dominant sheet and rill erosion estimation [13]. Esteves et al. [22] were the first to use PESERA in a forested area, followed by the work of other researchers [18,23,24].

Thus far, research needs required models to be able to represent the erosion mechanism in the most accurate manner possible, be overall flexible, reliable, and user-friendly tools, and have standardized input data [25,26].

Modern challenges, however, further mandate the need to (i) properly calibrate input data according to the local landscape characteristics and (ii) evaluate the simulated results, tackling the lack of direct erosion measurements, especially at the local or regional scales [27]. In this direction, specific parameter calibration attempts have been made at the international level for PESERA [28,29] and RUSLE [30], with parallel suggestions about the input data quality [21]. In Greece, indicative calibration efforts involve the work of Polykretis et al. [31] regarding the RUSLE R-/C-factor calibration in Crete and of Tsara et al. [19] regarding the PESERA soil-related input in Zakynthos Island and at the region of Spata. Concerning model validation, Sigalos et al. [32] compared the sediment volume measured in three cross-sections of the Giannoulas river, with soil loss being estimated by RUSLE. Efthimiou et al. [33] evaluated RUSLE outputs against the sediment discharge measurements recorded by the Greek Public Power Corporation (PPC) to four gauging stations in North-western Greece. Tsara et al. [19] evaluated the outputs of PESERA in three experimental transects extending 10 m along the hill slope. Rozos et al. [34] cross-evaluated erosion hot spots identified by RUSLE with the field-identified landslide-prone areas.

The principle that not all eroded material reaches the basin outlet has long been reported by Walling [35]. This is the reason why the Sediment Delivery Ratio (SDR) and Connectivity Indices (CI, aiming to locate potential sediment pathway obstacles such as depressions and sinks) concepts were developed and are long used. The index of connectivity (IC) introduced by Borselli et al. [36] provided the fundamental methodology following researchers, while Cavalli et al. [37] updated the main model by using different weightings. Unfortunately, several soil erosion models, PESERA and RUSLE included, cannot directly estimate the sediment yield delivered to a basin's outlet. Hence, the SDR index has to be employed when attempting to calculate net erosion.

However, the scarcity of spatio-temporally detailed input information at basin-level, and the labor-intensive calibration of the frequently data-hungry soil erosion models, call for the adoption of new approaches for the acquisition of semi-detailed field data. At large spatial scales, aerial photographs/orthoimages [38] are more appropriate for the investigation of erosion processes. Over the years, Remote Sensing (RS) has evolved into a valuable tool in soil erosion [39–43]. At smaller scales, soil surface (or volume) differencing through the successive recording of topographic changes is a different pathway to locate and quantify soil loss rates. The latter utilizes Terrestrial Laser Scanning (TLS) [44–47]—also known as terrestrial Light Detection and Ranging (t-LiDAR)—and Unmanned Aerial Vehicle (UAV) photogrammetry [48–53].

At the local scale, UAV imagery can bridge the spatiotemporal resolution gap between field investigation and RS observations [manned aircraft-based [54] or satellite-based].

UAVs are widely applied in the field of geospatial research and are involved, inter alia, in the study of soil erosion [48,50,55–57]. UAVs are commonly used in topographic change detection applications thanks to the newly emerged techniques and sensor evolution, resulting in highly efficient data acquisition [58,59]. This advanced and cost-effective technology has led to multiple research applications concerning landscape analysis and erosive process estimation [60–63]. The use of Structure-from-Motion (SfM) and multi-view stereopsis (MVS) enhances the capability of transforming a large number of overlapping images into 3D point clouds, Digital Terrain Models (DTM) and orthomosaics, even at mm-level accuracy [49,64–67]. Recent studies have highlighted the importance of cm-accuracy mapping and erosive process estimation through UAV imagery [68]. The temporal DEM or point cloud analysis can thoroughly estimate the volume of the eroded or depositional material through the volume difference of previously assessed and current surface reconstruction. Runoff pathways caused by extremely erosive rainfall events can now be highly delineated through the high accuracy of the UAV-SfM technique [69].

In light of the above, the study estimated soil loss at the anteceded reservoir of a sediment-retention dam (Platana dam) located in the broader Sperchios River watershed, Central Greece, using an empirical (RUSLE) and a process-based (PESERA) erosion model. Both models were found to estimate different erosion rates when compared to each other, while differences were also present within the same model simulation (e.g., the RUSLE simulation) when the C factor was altered.

The models' results were cross-evaluated against field measurements obtained by a UAV survey. The latter involved three campaigns performed during a two-year period (in August 2020, September 2021, and October 2022) and were utilized to develop two sequential topographic datasets of the reservoir. Their differencing deciphered into soil surface change and sediment yield, providing a highly accurate measurement of contemporary annual sediment deposition rates. Overall, this study tests the capabilities of the UAV-SfM technique in measuring high-resolution topsoil change detection.

2. Materials and Methods

2.1. Study Area

The research focuses on the well-defined reservoir of a sediment retention dam located in the northern mountainous part of the Sperchios watershed in central Greece, namely the Platana dam (Figure 1). Sperchios watershed is a graben-like asymmetrical depression as a part of a tectonic trough that separates the catchment into a northern and a southern part, with the latter being lifted and the former sinking. The watershed's (1820 km^2) vast quantities of sediment loads resulted in the gradually extending of the coastal delta area, which increased by approximately 135 km^2 in the last 6500 years, corresponding to a mean annual growth of 0.02 km^2/yr [70–72]. The study area is formed by a dense dendritic-type hydrographic network with drainage frequency values > 5.0 that reveal the impact of the existing geological formations, tectonic activity, and the high relief with steep slopes. The slopes vary from 0 up to 120% (mean value 55%) with a mean south aspect, which, when correlated with lithology, indicates an erosion-prone soil system. Moreover, the form factor, circularity ratio and length–width index values of the basin are low, contrary to the elongation ratio value, which is considered high, implying the presence of elongated basins with less side flow for a shorter duration and high main discharge, since the study area is tectonically active [73]. The total basin area is about 870 ha, covered mostly by shrubs, including a small portion of forest trees and agricultural land [according to Corine Land Cover (CLC) 2018 dataset]. The mean elevation is about 523 m a.s.l. Concerning the bedrock geology, the basin area is part of the Subpelagonian Geotectonic unit. The geological structure comprises the ophiolitic complex, including thick volcanic formations (meta-dolerites and basic tuffs), with localized Triassic–Jurassic limestones with cherts. The upland dam basin area consists of alluvial deposits of great thickness (Geological Sheet "Lamia", H.S.G.M.E, Athens, scale 1:50,000 [74]). Soil sample analysis was carried out to define the soil properties. Each sample was collected at a depth of 10–30 cm, in a sufficient

proportion for all the experiments to be carried out. Three soil samples were retrieved for every soil unit, while 6 samples were retrieved from the reservoir area to precisely estimate the Bulk Density (BD) of the deposition soil material. The soil analysis included the pH analysis, the electrical conductivity measurement, the granulometry test analysis according to Bouyoucos [75] and the soil organic matter content analysis according to Walkley & Black [76]. The USDA soil classification classifies the alluvial-related soils as Loamy soils (L), the calcareous soils are Sandy Loam (SL), and the volcanic soils are Clay Loam (CL) (Table A1, Appendix A).

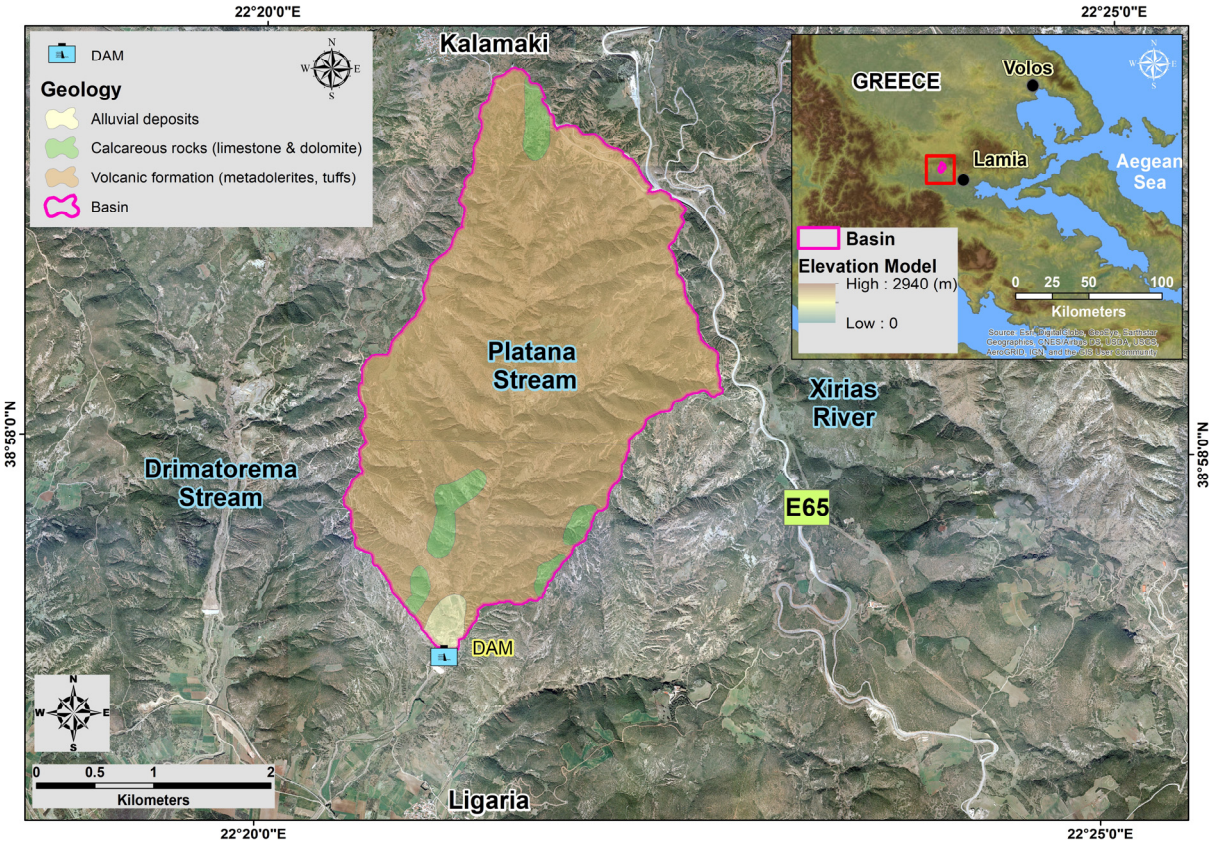

Figure 1. Geological map of the study area in Central Greece (Platana dam; scale 1:50,000) [74].

In this paper, the lowest downstream point of the main drainage area studied was defined as the basin's outlet located 150 m upstream of the dam.

The Platana dam is an embankment (rockfill with an impervious core) dam. Its features are presented in Table 1 and Figure 2.

Table 1. Platana dam characteristics.

Latitude (N)	350,206
Longitude (E)	4,313,396
Type	Earth Dam
Dam crest height (m)	205.50
Dam crest length (m)	208.00
Spillway crest length (m)	20.00
Maximum retention volume (m^3)	140,000

Figure 2. View of the Platana sediment retention dam features: perspective view of downstream slope (face) (**upper left panel**), upstream slope (**upper right panel**), reservoir (**lower left panel**), perspective view of the spillway and crest (**lower right panel**).

2.2. Data and Measurements

2.2.1. Earth Observation Data

UAV images: acquisition and processing: A DJI Phantom 4 quadcopter platform was used for the mapping needs of the study (Figure 2). The model was equipped with a $\frac{1}{2}$.3″ 12.4 MP with FOV 94°, 20 mm (35 mm equivalent) camera sensor and 4000 × 3000 image size. The operator took photos using nadir camera orientation due to the dam basin's flat surface in a predefined flight plan grid. The images were acquired when the UAV platform was in a still position. The automated flight plan led to consistent flight paths repeated on every flight. The minimum image overlap and the maximum forward and side overlap reached 75%, as other researchers also indicated in forestry areas [77–79]. Flight planning and operation were performed on DJI GS PRO. The minimum flight altitude was set to 18 m above ground level (AGL) with a 5 mm/pixel ground sampling distance (GSD). The first flight took place on 28 August 2020, the second on 16 September 2021 and an additional flight was made on 13 October 2022. In general, the flight altitude remained constant for all field surveys to achieve more accurate results. The flight surveys delivered 295 photos on 28 August 2020, 360 photos on 16 September 2021, and 232 photos on 13 October 2022. Additional photos during the second survey were required due to localized vegetation growth. During the first fieldwork, 15 ground control points (GCP) were used, while on 16 September 2021 and 13 October 2022, 23 GCP and 30 GCP, respectively (Figure 3), were finally selected for better image acquisition setup. The number of the GCP was based on the area extent. GCP setting and measurement can be really challenging in forestry and unreachable environments [80]. The GCPs were selected based on the shape and material

of the plate. We selected white, rectangular aluminum plates to avoid any deformation on the targets. The GCPs were spread across the study area, and their coordinates were retrieved by using a Spectra SP60 and SP85 Real-time Kinematic Global Navigation Satellite System (RTK GNSS), with a range accuracy of <1 cm in the horizontal plane and 1.7 cm in the vertical axis.

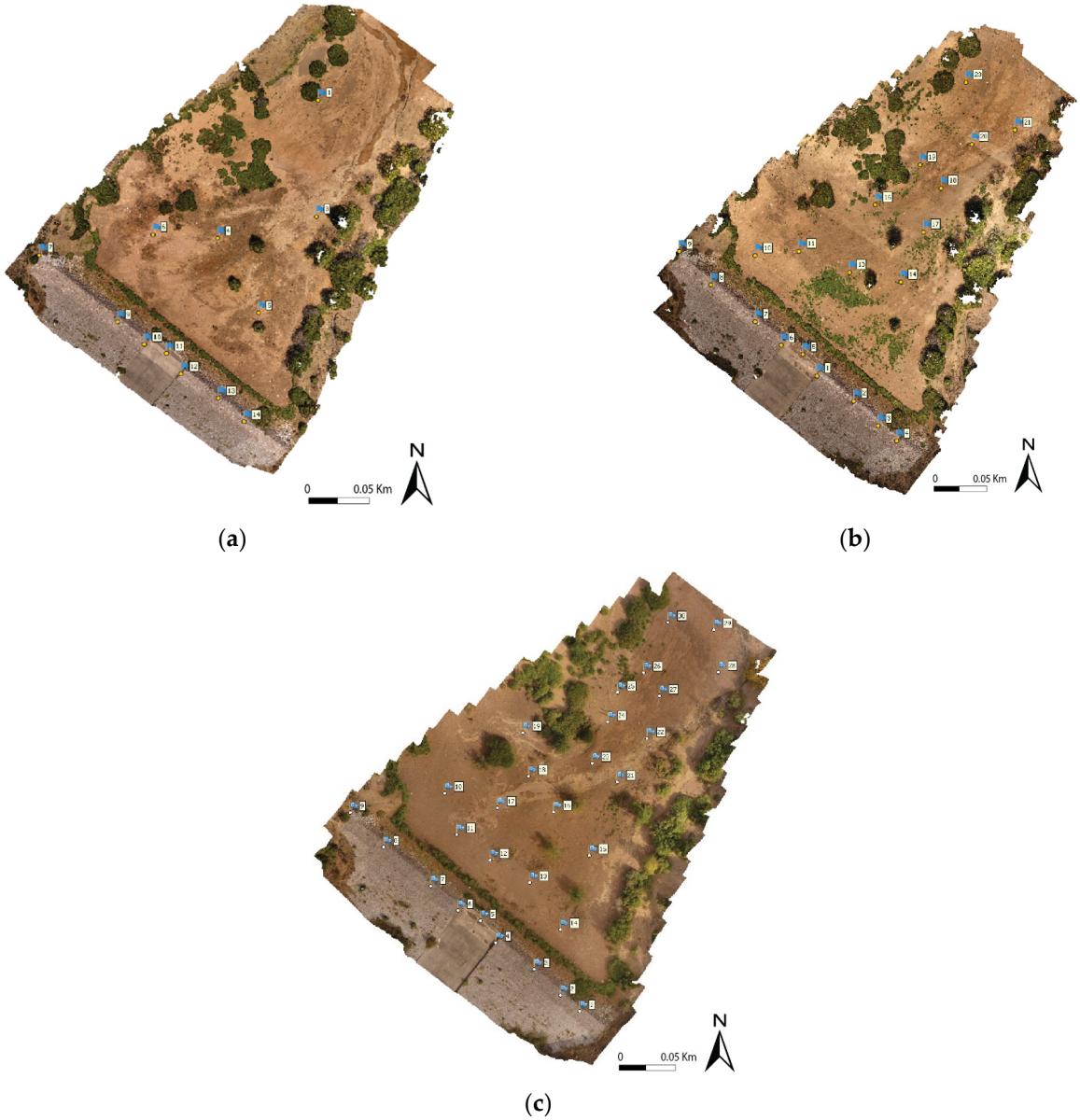

Figure 3. GCP locations on the three acquired orthomosaic images on (**a**) 28 August 2020; (**b**) 16 September 2021; (**c**) 13 October 2022. The numbering refers to the GCP location.

The sampling workflow comprised the (i) distribution of the ground control points (GCPs) over the study site, (ii) Sp85 GNSS GPS survey of the GCP points, and (iii) flight of the UAV mission. GCPs are used to translate and rotate the generated point clouds in a specific reference system [81], and their distribution constitutes a time-consuming part of the UAV survey [82]. Overall, the low flight altitude and the considerable overlapping provided high-resolution products.

The acquired images were photogrammetrically processed using Agisoft PhotoScan Metashape Professional (v. 1.5.5; http://www.agisoft.com/downloads/installer/, accessed on 16 September 2020). The complete study workflow is summarized in Alexiou et al. [44].

To conclude, all data were processed in the high-accuracy mode for the alignment, the dense cloud derivation and the mesh, texture, and tiled model production. Conclusively, the photogrammetry workflow comprised the (i) data selection, (ii) appropriate image selection, (iii) image alignment and dense cloud development (high quality and mild filtering definition), (iv) detailed surface (mesh and texture) and tiled model development, (v) adding and checking the markers (same name and coordinate system as the GCP), (vi) checking the markers' error, (vii) development of the DEM, and (viii) export of the point cloud (Figure 4), DEM and orthomosaic. The low-altitude flight and the significant overlapping resulted in high-resolution products (Table 2).

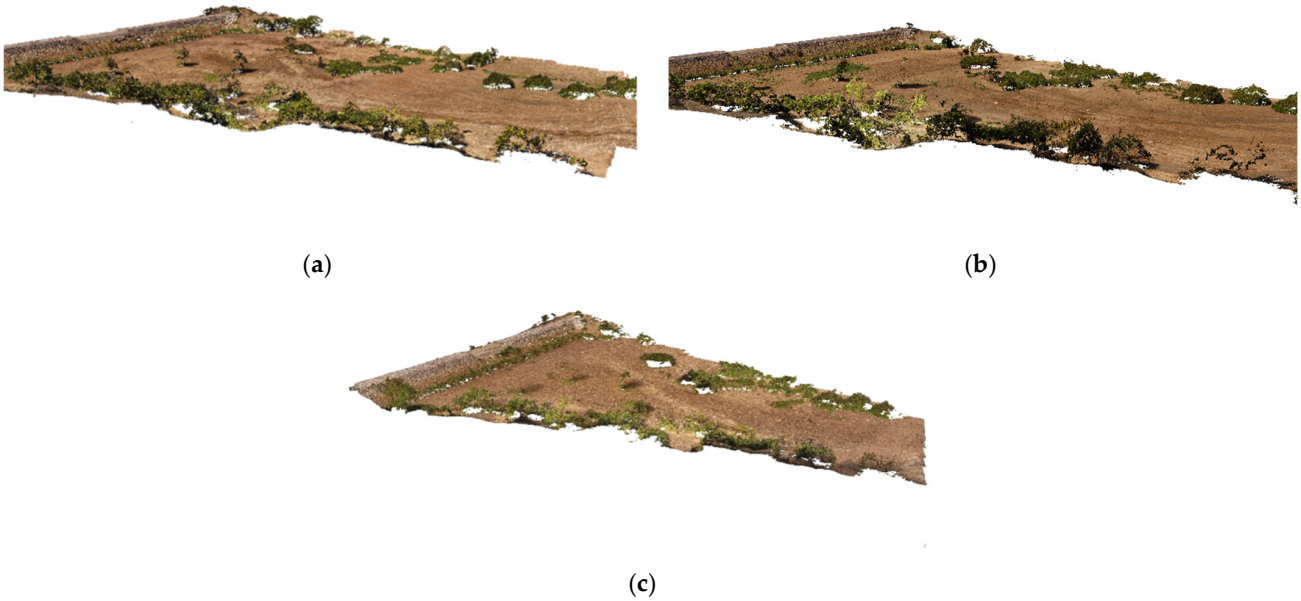

(**a**) (**b**)

(**c**)

Figure 4. Agisoft 3D model based on DJI Phantom 4 UAV surveys on (**a**) 28 August 2020; (**b**) 16 September 2021; (**c**) 13 October 2022.

Table 2. Agisoft products resolution (mm/pixel).

	Resolution mm/pix		
Product	**28 August 2020**	**16 September 2021**	**13 October 2022**
Tiled model	10	7	10
DEM	20	14.8	17
Orthomosaic	10	7.4	8.6

Subsequently, the point clouds between the two surveys (2020–2021 and 2021–2022) were compared using the CloudCompare software (version 2.6.1; https://www.cloudcompare.org/doc/, accessed on 20 October 2022). The point cloud analysis was considered to be more appropriate for soil surface change detection since, in 3D space, a point-to-point comparison would perform better than that of the derivative DEMs by avoiding the interpolation of the 2D data required when assessing DEM differentiation in three dimensions [83]. The software offers a user-friendly environment, saving computational time by reducing the total volume of data using a specific Octree structure. In this context, during our research, in order to achieve a clear point cloud with sufficient point density, we chose to manually remove (i) the cloud noise, (ii) points exceeding the area of interest, (iii) remaining vegetation traces, (iv) incorrectly placed points within the cloud due to UAV-SfM issues (e.g., dust points in the air). Afterward, the clouds were 'registered' in the software by correlating/aligning their points with the already stable GNSS-identified GCPs. The high alignment accuracy achieved indicated the adequacy of the GCP number used in the study. Finally, the comparison was performed utilizing the model-to-model cloud comparison (M_3C_2) algorithm/plugin, allowing for (vertical) distance computation between clouds

in accordance with the natural surface of the site [84]. According to Lague et al. [84], the algorithm combines the local distance of two-point clouds in correlation with normal surface detection, which tracks 3D variations in surface orientation. This algorithm has the advantage of operating directly on point clouds and estimating a confidence interval depending on point clouds' characteristics and registration error. After the experimental use of different values and the "guess params" option (provided by the software), we concluded with a 0.30 m normal scale diameter and a 0.20 m projection scale diameter. All of the points of the defined "point cloud #1" were used as core points for normal calculations.

Normalized Difference Vegetation Index (NDVI): The NDVI was used for the land cover condition assessment required by the PESERA input data (monthly vegetation coverage estimation) and the FVC index (described below). This index expresses the difference between wavelength reflectance in two portions of the electromagnetic spectrum, the visible Red and the near-infrared [85], corresponding to the relative vegetation properties. NDVI acquires values in the range −1 (no vegetation) to +1 (dense vegetation).

Fraction of Vegetation Cover (FVC): The FVC corresponds to the percentage of the green (photosynthetically active) vegetation vertical projection over the reference ground area, which has already been applied in monitoring soil erosion [86–88]. Compared to the uniform vegetation coverage, which is typically assigned, the FVC enables more detailed specification of the inter-monthly vegetation variations, which are tightly related to the soil erosion processes [89], offering a more accurate estimate of coverage percentage. The widely used NDVI is considered less suitable for change detection over time since atmospheric correction is required. Particularly in the Mediterranean area, the atmospheric correction of the Remote Sensing (RS) products is exceptionally challenging due to the highly fragmented landscapes and the multi-level changes in the vegetation coverage throughout the year [90]. It is highly appropriate for monitoring ecosystems and supporting service assessments at different spatiotemporal scales [91]. Technically, the FVC is a re-normalization of the reflected near-infrared light (700–1100 nm), which is captured by modern multispectral sensors [92]. FVC can be calculated as a function of NDVI according to the 'two-end members' formula of Zeng et al. [93] (Equation (1)). The $NDVI_o$ and $NDVI_{full}$ can be estimated as the minimum and maximum NDVI values since they depend on the study area soil and vegetation types [94,95]. $NDVI_{full}$ coincides with the highest NDVI value during the wet period.

$$FVC = (NDVI_x - NDVI_o)/(NDVI_{full} - NDVI_o), \quad (1)$$

where $NDVI_x$ is the monthly NDVI value, $NDVI_o$ is the NDVI value for bare soil, and $NDVI_{full}$ is the NDVI value of a fully vegetated area.

2.2.2. Geospatial Data

Meteorological data were acquired by the National Observatory of Athens (NOA) for the gauging station of Makrakomi covering three periods, the years 2020, 2021, and 2022. The climatic data comprise daily time series of rainfall (30 min resolution), temperature, and potential evapotranspiration. The station location is considered to adequately cover the area of interest, being representative of the local climatic conditions.

Annual precipitation for each application was 572.0 mm (September 2020 to August 2021) and 793.2 mm (October 2021 to September 2022) (Table 3). The variable's temporal resolution is controlled by the catchment's climate pattern. Rainfall depth displays distinct seasonal variation evolving in clear cycles, typical of the Mediterranean climate. At the mean monthly scale, its fluctuation within a calendar year is depicted by an inverse bell distribution, acquiring its highest values in the winter (left/right tail) and the lowest in the summer (bottom of the curve). In the first period, between the 2020 and 2021 surveys, the minimum rainfall value was recorded in May 2021 (2.0 mm), a turning point of the 'hydrological year'-like regulation after which precipitation started to decrease entering the warm season of the year (June to September), and the maximum in September 2020 (148.2 mm). In the second period, i.e., between the 2021 and 2022 campaigns, minimum

and maximum precipitation were yielded in September 2022 (2.0 mm) and December 2021 (155.8 mm), respectively.

Table 3. Precipitation values (in mm).

Period	Sep	Oct	Nov	Dec	Jan	Feb	Mar	Apr	May	Jun	Jul	Aug	Sep	Total
09.2020–08.2021	148.2	33.6	9.8	84.0	91.4	46.6	58.6	49.2	2.0	30.2	7.6	10.8		572.0
10.2021–09.2022		115.8	133.8	155.8	76.6	53.2	60.8	26.4	49.2	71.2	28.8	19.6	2.0	793.2

Topography and geology delineation were based on a 5 m DEM and a local geological map, respectively. Detailed soil mapping, fieldwork, and laboratory soil analysis were conducted in order to define pedological properties. Soil depth, rock fragments, and soil texture were also assessed for each soil unit. The land use coverage estimation was based on fieldwork and the CLC database. The land use was depicted using the novel high-resolution map of Efthimiou et al. [91] (see their Figure 6). This hybrid dataset was developed using as base-layer the 2018 CLC database, upgraded in its agricultural areas by the integration of the Land Parcel Identification System (LPIS) [96] and Beneficiaries Declarations (BD) inventories' elemental/reference features, namely ilot polygons (European Court of Auditors, 2016) and individual farmlands, respectively. The sequential geospatial fitting of the participating registries (GIS layers) as BD, ilot → BD-ilot → BD-ilot, CLC → BD-ilot-CLC led to the progressive update of the individual datasets' cultivated parcels. Classification harmonization was achieved by matching the ilot and BD nomenclatures to the CLC registry. Overall, the new map comprises CLC features, ilot polygons, and BD parcels. The basin is mostly covered by shrubs, including a small portion of forest trees and agricultural land (Figure 5, Table 4).

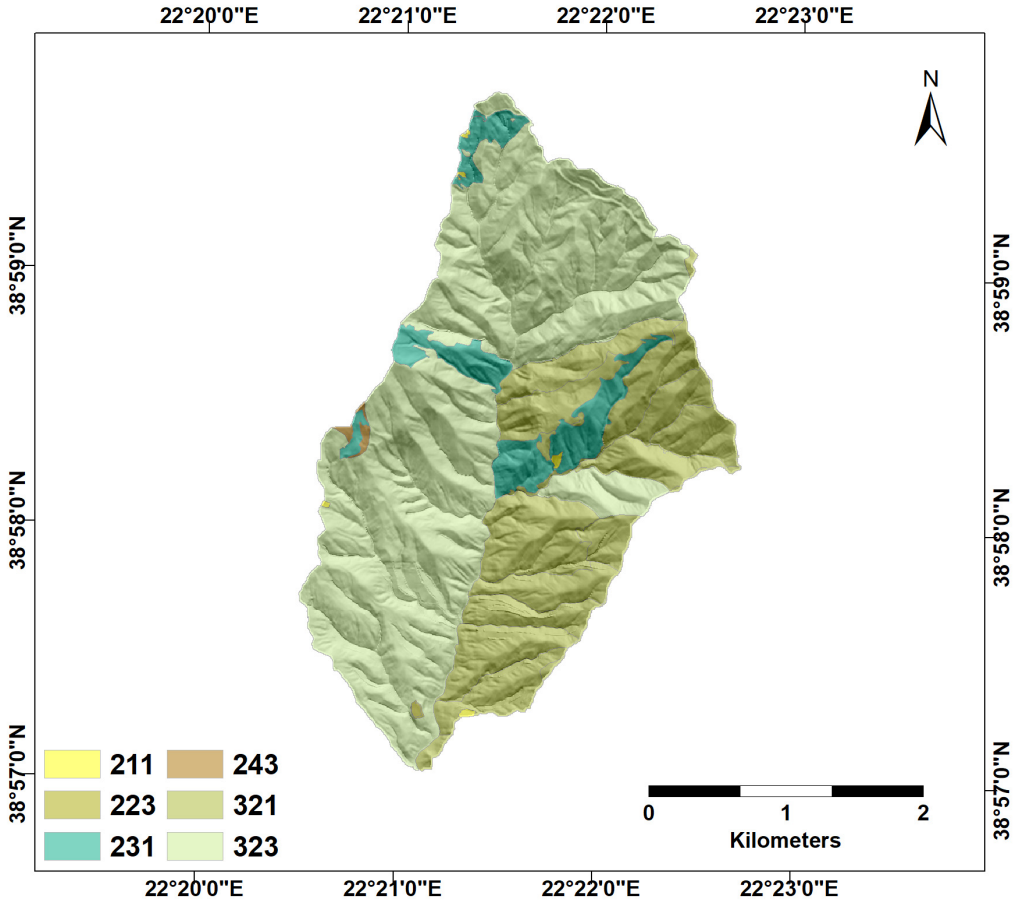

Figure 5. Land use classification of the Platana Dam basin (see Table 4 for code descriptions).

Table 4. Land use classification of the Platana Dam basin delineation and respective RUSLE C-factor values.

Level 1	LULC * Level 3 [a]	Status	Area (km^2)	C-Factor
Agricultural areas	211	Arable	0.019	0.3
	223	Non-arable	0.009	0.1
	231	Non-arable	0.669	0.02
	243	Non-arable	0.027	0.07
Forest and semi-natural areas	321	Non-arable	2.734	0.05
	323	Non-arable	5.231	0.03

* Land use/Land Cover; [a] 211: Non-irrigated arable land, 223; Olive groves, 231; Pastures, meadows, and other permanent grasslands under agricultural use, 243; Land principally occupied by agriculture, with significant areas of natural vegetation, 321; Natural grasslands, 323: Sclerophyllous vegetation.

2.3. The Pan European Soil Erosion Risk Assessment (PESERA) Model

The PESERA model [13,14] was initially developed for average annual water erosion assessment in agricultural areas at the European level. It is a physical-based model, suitable for large watersheds and regional scale applications [21]. As it can be applied on different spatial scales (hillslope, regional or national), it is often used in the Mediterranean [18,97,98], where detailed data are available and more detailed distributed soil erosion rates estimation is required. PESERA is based on the precipitation division into overland flow and infiltration. Sediment yield is calculated from runoff and each storm event, resulting in the dominant sheet and rill erosion estimation [13]. Permanent gully, channel erosion, channel delivery processes, and channel routing are not considered [14]. The model estimates soil erosion as (Equation (2)).

$$E = k\Delta\Omega, \quad (2)$$

where E is soil loss in t ha^{-1} y^{-1}, k is the erodibility based on land use, soil parameters, and vegetation cover, Δ is the topographic factor, and Ω is the runoff/climate/vegetation soil erosion potential. Ω is based on the gridded climate data, vegetation cover, water balance, and plant growth [14]. Input data requirements include land use and land cover, soil parameters, climatic and topographic records. Overall, 128 input data layers are built by the model and compiled in a single final layer.

2.4. The Revised Universal Soil Loss Equation (RUSLE) Model

The RUSLE is an empirically based soil erosion model originally developed for agricultural areas in the United States. It has been widely used for the spatial distribution of soil erosion in the Mediterranean [32,99,100]. It estimates soil loss (A, t ha^{-1} y^{-1}) as the linear product of five coefficients (Equation (3)), namely the rainfall erosivity (R-factor, in MJ mm ha^{-1} h^{-1} y^{-1}); soil erodibility (K-factor, in t ha h ha^{-1} MJ^{-1} mm^{-1}); topographic (LS-factor, dimensionless); cover management (C-factor, dimensionless); and conservation practice (P-factor, dimensionless) factors. The R-factor is the climatic component, accounting for the effect of rainfall on soil loss. The K-factor represents soil's vulnerability against the abrading action of rainfall and overland flow. The LS-factor is the model's topographic component. The C- and P- factors simulate the protective effect of land cover and conservation measures against soil erosion, respectively (Equation (3)).

$$A = R \times K \times LS \times C \times P, \quad (3)$$

2.5. The Sediment Delivery Ratio (SDR) and Connectivity Index (CI)

The Sediment Delivery Ratio (SDR) and the Connectivity Index (CI) are empirical tools developed to address the problem of not all of the eroded material reaching the basin outlet [35], aiming to overcome potential sediment pathway obstacles, such as flow sinks and depressions (deposition areas). This is a common method applied in erosion modeling due to the absence of net erosion rate estimation. CI development is based on topography,

surface roughness, and land cover [36,37,101,102]. SDR is related to the upslope area, climatic conditions, and the shape and slope of the catchment.

The Borselli et al. [36] CI approximation was used in the present study (Equation (4)) since it was established in a medium-sized watershed under similar Mediterranean conditions (in Tuscany, Italy). The index was compiled in a Geographic Information Systems (GIS) environment, utilizing the ArcMap 10.5 suite (Figure 6). The RUSLE C-factor was used as a proxy of surface roughness, delineated as in the RUSLE implementation [36,103,104].

$$\mathrm{IC_k} = \log_{10}\left(\frac{D_{up,k}}{D_{dn,k}}\right) = \log_{10}\left(\frac{\overline{w}_k \overline{S}_k \sqrt{A_k}}{\sum_{i=k,n_k} \frac{d_i}{w_i s_i}}\right) \quad (4)$$

where $D_{UP,k}$ is the upstream component, $D_{dn,k}$ is the downstream component, W_k is the weight of the k cell (where W = C_{RUSLE} factor), A_k is the upslope area (m^2) S_k is the slope gradient of the cell, and d is the length of the cell.

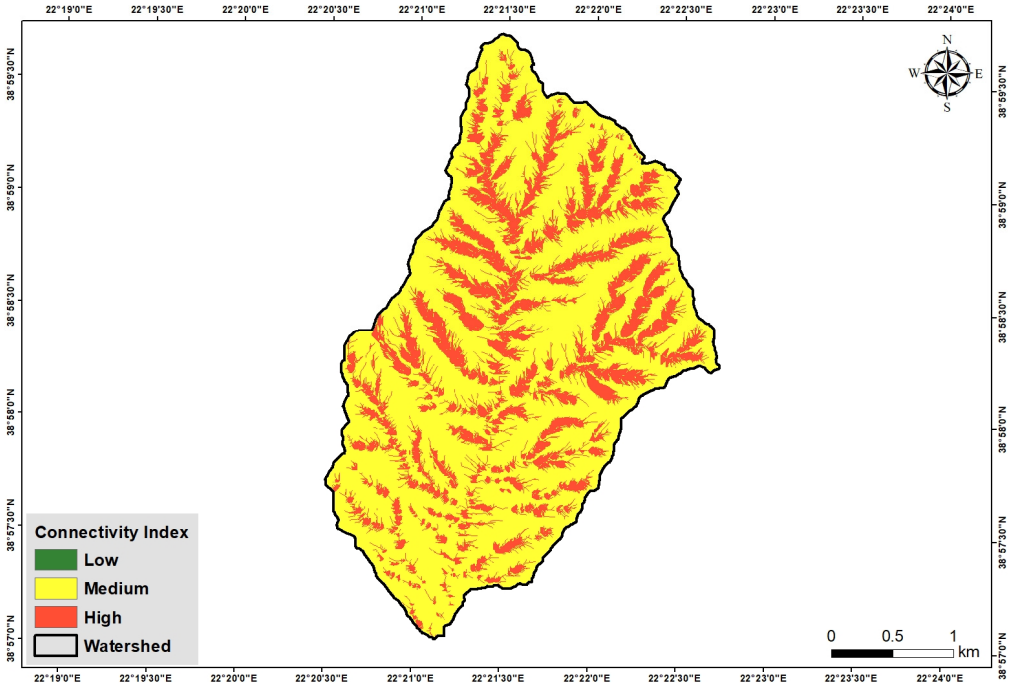

Figure 6. Connectivity Index map, showing medium and high connectivity across the study area, resulting in the absence of significant sinks, and the rise in soil erosion potential.

The land use and the topography (absence of sink areas) control the sediment routing to the main channel. Figure 6 shows that the basin is characterized by a medium to high connectivity index due to the dense stream network and the steep slope, implying that most sediment can be delivered to the outlet through the dense stream network.

The SDR formulas tested [105–108], yield an index range of 35% to 45%, hence the mean value of 40% was selected (Equations (5)–(8)).

$$\text{Log (SDR)} = 1.8768 - 0.14191 * \log(10 * \text{A}) \text{ (MANER 1962, A is the area in mi}^2\text{)}, \quad (5)$$

$$\text{Log (SDR)} = 1.7935 - 0.1419\log(\text{A}) \text{ (Renfro 1975, A is the area in km}^2\text{)}, \quad (6)$$

$$\text{SDR} = 0.51 * \text{A}\hat{}- 0.11, \text{ (USDA 1975, A is the area in mi}^2\text{)}, \quad (7)$$

$$\text{SDR} = 0.42 * \text{A}\hat{}- 0.125 \text{ (Vanoni, 1975, A is the area in mi}^2\text{)}, \quad (8)$$

The complete study workflow is summarized in Figure 7.

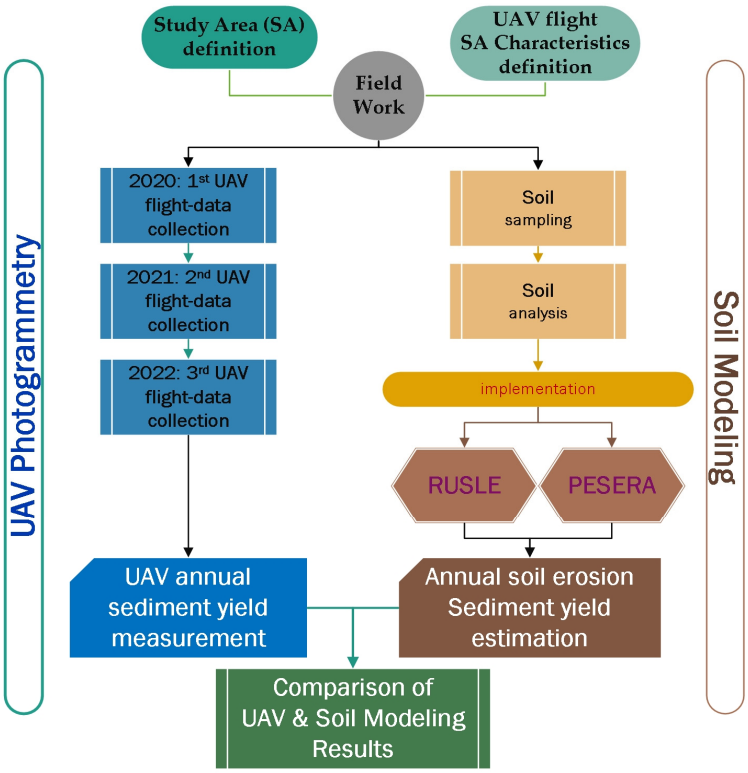

Figure 7. Complete survey workflow.

3. Results

3.1. UAV Photogrammetry and Measurement of the Actual Deposition at the Retention Dam

UAV photogrammetry was applied in order to measure the real annual deposition at the retention dam. In particular, a point-to-point comparison of the two campaigns' (data collected in 2020, 2021, and 2022, resulting in two study campaigns, e.g., 2020–2021 and 2021–2022 datasets) point clouds led to the calculation of the annual topsoil change (Figures 8 and 9). The point cloud difference revealed a significant topsoil deposition, consistent with the strong sedimentation observed during the 2021 and 2022 fieldwork. The analysis shows significant upland soil mass movement, reaching the dam and gradually accumulating behind the upstream slope.

The annual sediment distribution change is obvious in Figure 10, where the originally even sediment distribution (approximately 100 m) behind the dam in 2020 DSM was interrupted by the new stream pathway, revealing a more intrusive sediment deposition in 2021 and 2022 DSM. The initial surface was cannibalized by the stream erosional process, resulting in a new redistribution closer to the dam. This is attributed to the 2021–2022 rainfall events (see also Table 3), where almost a 40% increase in precipitation occurred within the last year of observation (2022). Additionally, the low-height vegetation along the surrounding area of the dam in 2020 DSM, during the next year of data collection, was found buried under a large volume of sediment.

During the second data collection (September 2021), vegetation cover (low-height grass) was denser in some areas, making vegetation point removal more demanding and time-consuming. However, the watershed's mean vegetation cover was stable (65%) for all campaigns. The defined data acquisition UAV-SfM setup is considered appropriate for this type of research, according to the error estimation analysis. The defined low flight height (<18 m) and the high accuracy data collection (in correlation with GSD) resulted in highly detailed derived products with mm-scale (3D tiled model accuracy less than 1 cm).

The application of the M_3C_2 algorithm results in a mean annual vertical 0.27 m rise of the topsoil surface at the stream outlet during the first simulation and 0.36 m for the 2021–2022 simulation. In Figure 8, the sediment deposition pattern is straightforward and

can be related to the stream flow. The red flow towards the retention dam indicates the areas where sediment deposition and maximum values are observed. Figure 8 shows the spread of the newly annual arrived sediments, initially more localized along the stream, then widely scattered as approaching the dam. In Figure 9, the sedimentation is not totally controlled by the stream, as a wide sediment distribution is visible at the right part of the dam. The SfM technique yielded an annual volume change of about +1620 m^3 and 3500 m^3, covering a total (dam upland) area of 6000 m^2 and 9700 m^2 for each study, respectively (2020–2021 and 2021–2022). The unoccupied areas in the M_3C_2 visualization (black areas) are caused by the tree canopy obscuring the area, which were chosen not to be interpolated to decrease volume estimation errors.

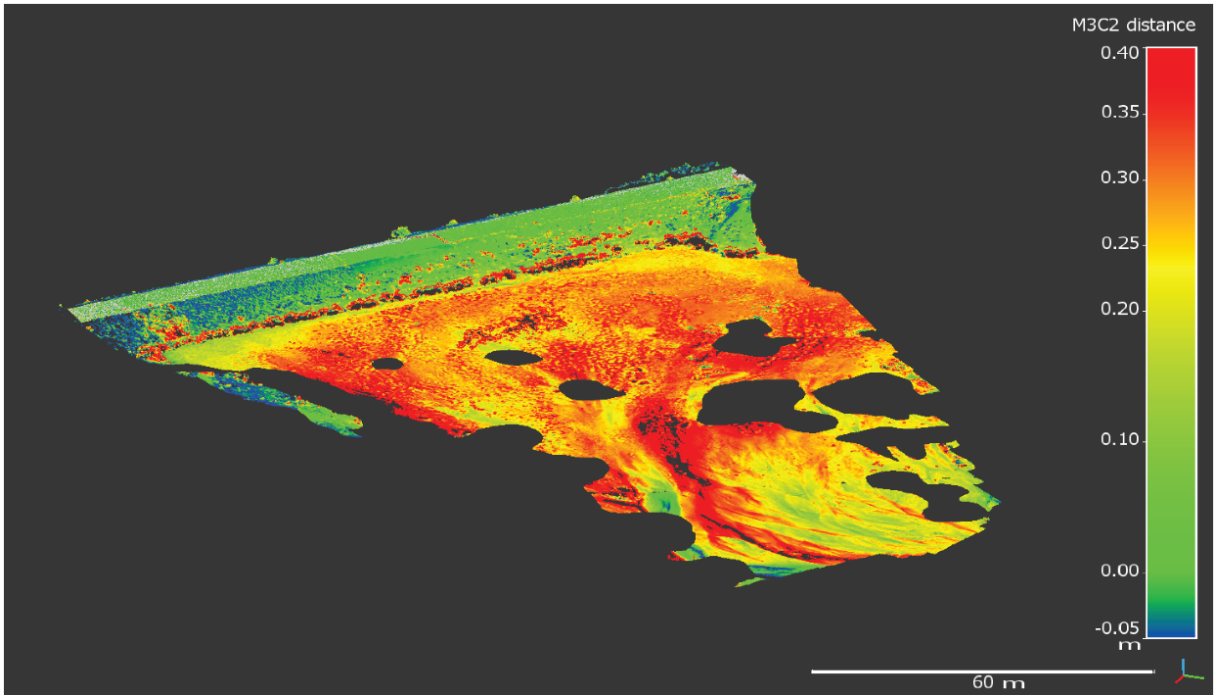

Figure 8. Annual topsoil vertical difference estimated using the M_3C_2 algorithm application (2020–2021).

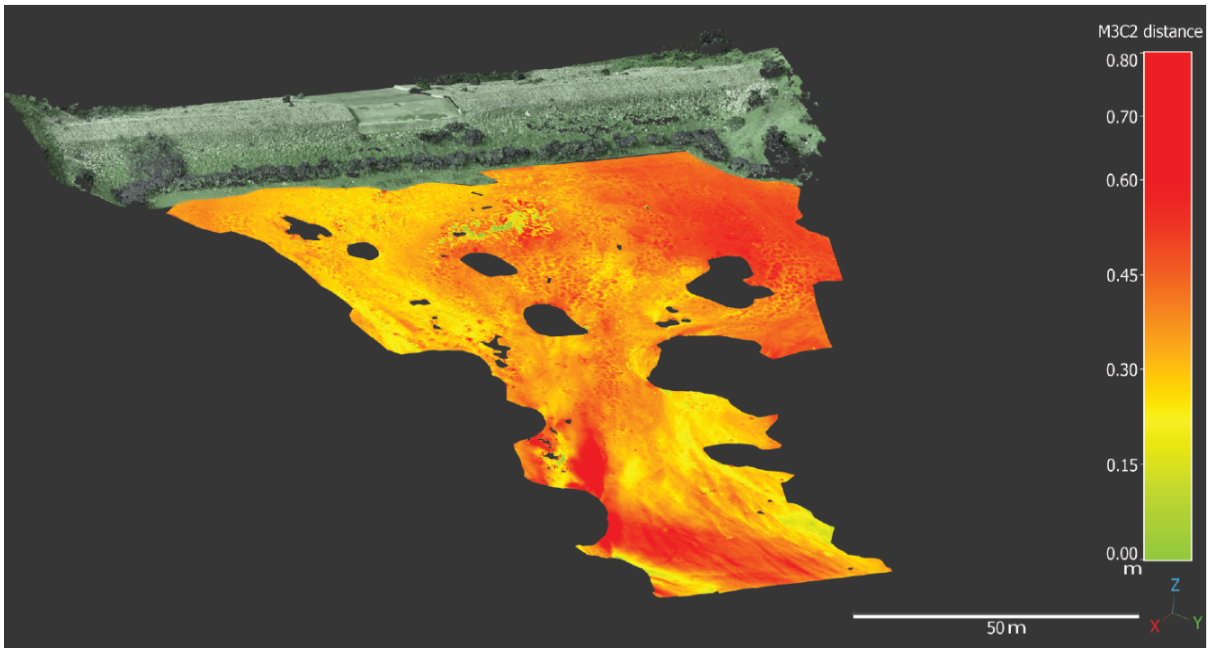

Figure 9. Annual topsoil vertical difference estimated using the M_3C_2 algorithm application (2021–2022).

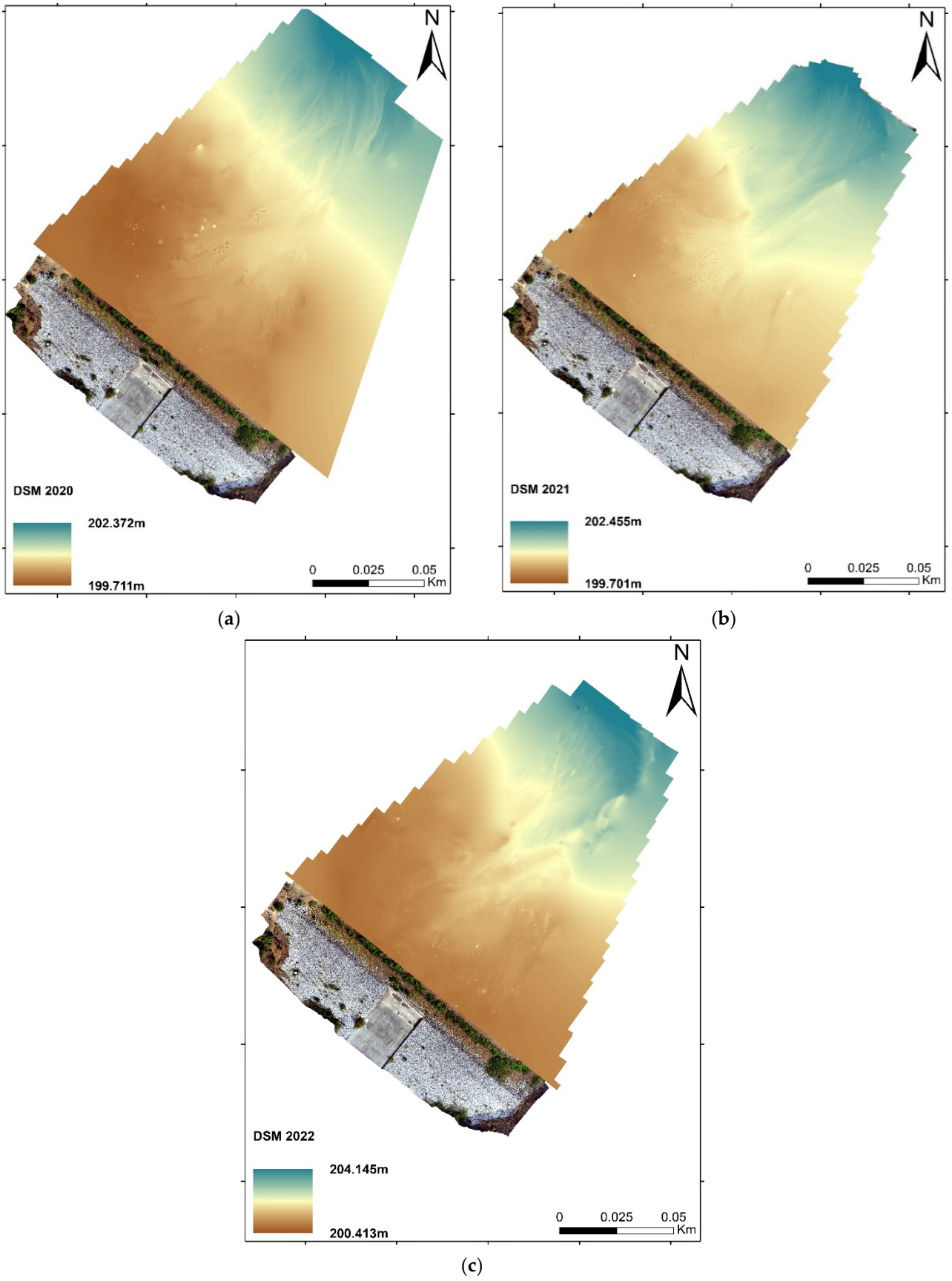

Figure 10. DSM (0.02 × 0.02 m pixel size) interpolated for error evaluation. (**a**) 28 August 2020; (**b**) 16 September 2021; (**c**) 13 October 2022.

Concerning the final measurement errors, four GCP were used for XYZ accuracy assessment by comparing their XYZ coordinates extracted from the point cloud with the actual coordinates, as measured in the field using the RTK GNSS. The GCP used were selected based on their location. We also selected GCP based in the central area where the main deposition seemed to take place and to be able to estimate any probable dome effect error of the UAV-SfM model that may occur. During the second field study in 2021, we placed more targets within the previously delineated study area to avoid any central dome deformation of a flat area. The final model error was slightly reduced (−0.01 m), so the 2021 GCP grid was considered more appropriate, and more GCP were placed during the last study (2022). Low accuracy was observed towards the boundaries, where fewer photos were aligned to the model. According to the XYZ GCP error analysis, a range of 0–0.03 m mean error was calculated. The registration errors of the point clouds ranged from 0.02 to 0.04 m. Conclusively, we resulted in a 0.03 m measurement error for the 2020–2021 dataset and 0.02 m for the 2021–2022 dataset. The error analysis in correlation with the total measured area of 6000 m^2 (2020–2021) and 9700 m^2 (2021–2022) leads to the volume error estimation of about ±180 m^3 and ±194 m^3, respectively.

For a complete error estimation, we additionally calculated the error, including the vegetation removed areas (+1650 m^2 for 2020–2021 and +2800 m^2 for 2021–2022, Figure 10a–c) by interpolating the mean surrounding sediment deposition value. The sediment volume reaches 2065 m^3 considering an error of ±275 m^3 (2020–2021) and 4500 m^3, considering an error of ±437 m^3 (2021–2022).

3.2. The PESERA Application

The PESERA model was used to simulate soil erosion for the years 2020, 2021, and 2022, in a 5 × 5 m grid, based on the available 5 m DEM. The soil and land use-related parameters were specified based on the 1997 Ministry of Rural Development and Food (1:50,000) and the 1:30,000 Misopilinos 2015 AUTH Lamia's soil map, the geological map (Geological Sheet "Lamia", H.S.G.M.E, Athens [74]) and the CLC 2018 land use map, and they were validated by in situ inspection, soil sampling and laboratory analysis by the authors (Table A1, Appendix A). All of the input parameters were translated into suitable PESERA model layers based on the correspondence provided by Gobin & Govers [29]. The PESERA application is thoroughly described in Appendix A.

One model application per year was made, resulting in an annual soil loss of 1.12 t/ha and 2.5 t/ha (Figure 11a,b) for 2020–2021 and 2021–2022 simulations, respectively. A high mean 0.44 t/ha soil loss value of September 2020 has been extracted, but it is attributed to the rainfall event of 18 September 2020, when, following a dry summer period, a high-depth precipitation occurred (88 mm of rain on 18 September 2020 and 23 mm on 19 September 2020), resulting in an extreme flood event related to Ianos Medicane. Ianos was a rare tropical-like cyclone that caused severe damage in central Greece [109].

The classes of the degree of soil erosion corresponding to the ranges of soil erosion rates were defined according to Kirkby et al. [14]. The moderate erosion-prone area corresponds to areas where the delimiting slopes are greater and the soil type is more susceptible to erosion (Figure 8b), while the slight erosion class corresponds to more flat areas. The mean bulk density value of 1.3 t/m^3 was used for the sediment yield estimation (for both models) according to the soil textural classes identified [110,111]. The total PESERA sediment volume estimate that reached the outlet was 300 m^3 for the year 2020–2021 and 670 m^3 for 2021–2022, following the 40% SDR application.

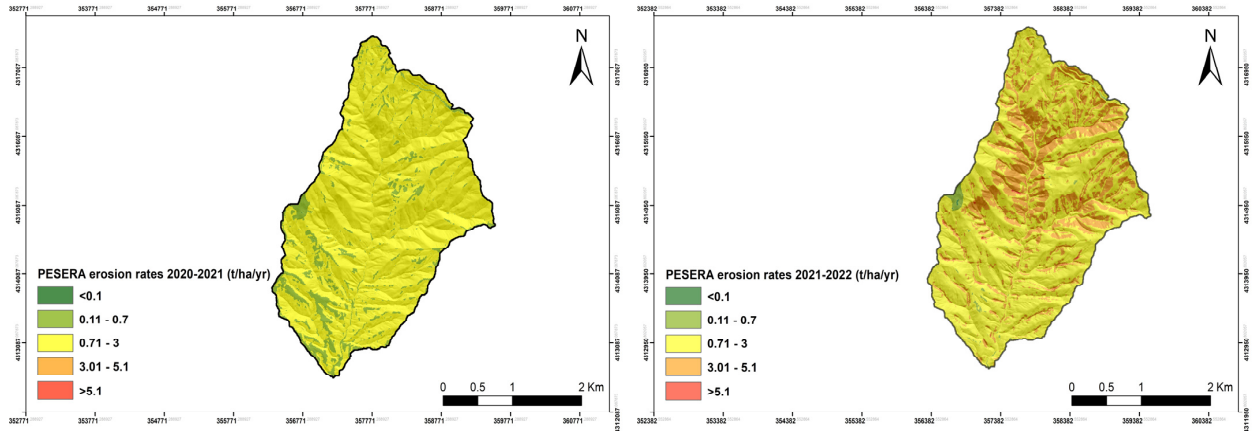

(**a**) (**b**)

Figure 11. PESERA erosion rates (t ha^{-1}) (**a**) from September 2020 to August 2021, (**b**) from October 2021 to September 2022.

3.3. The RUSLE Application

Mean source erosion was estimated as the linear spatial product of RUSLE's individual factors (Figure A2, Appendix B) for the 2020–2021 and 2021–2022 simulations. All of the layers were delineated at 5 m spatial resolution. The RUSLE application is thoroughly described in Appendix B.

Mean annual soil loss (gross erosion) was estimated at 3.51 t ha^{-1} y^{-1} (2020–2021) and 3.56 t ha^{-1} y^{-1} (2021–2022) (Figure 12a,b). Since RUSLE cannot directly estimate the sediment yield delivered to the basin outlet, the SDR (40%) was used, and net (transported gross) erosion was estimated by multiplying the index by the source soil loss. The outcome was 937 m^3 for the first simulation and 953 m^3 for the 2021–2022 simulation of soil delivered to the basin outlet.

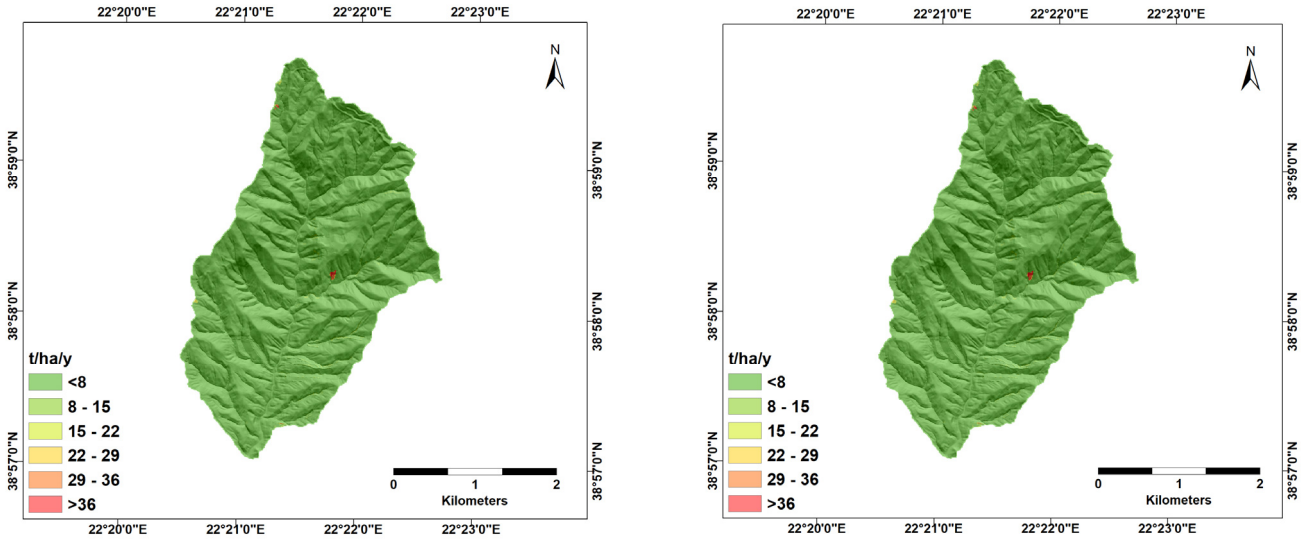

(**a**) Gross soil erosion 2020–2021 (**b**) Gross soil erosion 2021–2022

Figure 12. RUSLE erosion rates (t ha^{-1}) (**a**) from September 2020 to August 2021, (**b**) from October 2021 to September 2022.

4. Discussion

The availability of soil loss records is mandatory for sediment control management [112]. However, the uncertainty that characterizes the outputs of contemporary soil erosion models [26,27] hinders the design of appropriate mitigation strategies.

Our application clearly demonstrates that the gap between field measurements and sediment modeling can be bridged by the UAV-SM method. UAV and photogrammetry technique is considered a highly efficient and affordable tool for high-resolution spatial analysis/change detection [54,69,113,114]. Additionally, point clouds and UAV-SfM methods are the baseline for the production of 3D models for surface reconstruction, surface change detection, and soil erosion monitoring [44,82,83,115]. The 3D point-to-point analysis leads to high-accuracy results in several scientific applications regarding surface change detection [45,50,116,117]. This multi-vector analysis denotes the complexity of the microsurface, which cannot be accurately represented by 2.5D DEM data and the interpolation method [83]. The M_3C_2 algorithm that we selected as the baseline for surface change detection is currently used in a broad field of geo-research applications, such as landslides, flood events, post-fire erosion, and forests [44,45,118–120]. In this study, we managed to achieve a cm-accuracy of the microsurface reconstruction, leading to high-accuracy sediment pathway and distribution delineation.

Caution should be taken during the 3D reconstruction (SfM software application) since it entails a complex error behavior; thus, measurements for error estimation are vital during the complete study procedure. We estimated a 0.03 m error through the XYZ GCP error analysis, while an error of 0.02 m was calculated during the registration of point clouds. Wang et al. [115] found similar RMSE of 1.1 to 3.83 cm by using Phantom 3 UAV. Such low errors estimation was a consequence of the low flight height, the optimized overlapping, and the proper vegetation removal (the presence of vegetation leads to data occlusion, i.e., gaps in the measured point cloud due to shadowing, and is considered the most obstructing factor in the application of UAV-based photogrammetry for soil erosion estimation). These values are within the accuracy margins reported by other similar studies, e.g., 0.1–0.15 m [116], 0.03 m [48], and 0.025–0.04 m [64,67]. Increasing GCP within our study area led to a decrease in the total accuracy error by 33.3% [121,122]. For this study, height flight and nadir image capture were selected in accordance with the flattery environment and the simple anaglyph pattern.

We measured a mean annual surface increase of 0.27 m, resulting in a mean deposition of 1620 $m^3 \pm 180$ m^3 or 2065 $m^3 \pm 275$ m^3 (including the vegetated areas) for the 2020–2021 research. The 2021–2022 measurements revealed a significant increase at the entire dam upland basin, reaching a mean value of 0.36 m, resulting in a mean deposition of 3500 $m^3 \pm 194$ m^3 or 4500 $m^3 \pm 437$ m^3. By applying the BD and SDR defined, these values correspond to a mean erosion rate of 6 t ha^{-1} and 13 t ha^{-1} for the 2020–2021 and 2021–2022 simulation years, respectively, for the total watershed. Neugirg et al. [50] measured similar sediment deposition of 2000 m^3 by applying the DoD method of both UAV photogrammetry and TLS techniques at a 125,000 m^2 catchment. Other researchers have concluded a mean annual gully erosion rate of 0.58 t in 18.65 m^2 of the detailed monitored area and 5.25 t covering an area of 17.45 m^2 [82], highlighting that photogrammetry is appropriate for erosion quantification. Wang et al. [115], by monitoring gully erosion, calculated an annual volume change of 9.66 m^3 through DTM temporal comparison.

Regarding the soil erosion simulation, both modelling approaches, PESERA and RUSLE, were able to identify hotspots/areas of land degradation. Both models appear to underestimate the mean annual erosion rates. Specifically, mean erosion for the period September 2020–August 2021 was estimated at 3.51 t ha^{-1} by RUSLE and at 1.12 t ha^{-1} by PESERA. Waltner et al. [123] also state that when PESERA is applied in high spatial resolution, as in the case of this study (5 m grid), it delivers lower than expected erosion rates, a fact that explains the underestimation of the actual field measurements. Similar results of PESERA underestimation were also validated in Mediterranean environments [28,124,125], while Sigalos et al. [32] found similar values for RUSLE erosion rates compared to measured stream section measurements. In van Rompaey et al. [28], the validation method was based on measured sedimentation volumes in reservoirs. Stefanidis et al. [126] implemented the RUSLE model, resulting in an average value of 6.15 t ha^{-1} in Crete. Our PESERA values are in accordance with Spain rates in similar Mediterranean conditions reported by de

Vente et al. [127] and Cerdan et al. [128], with an estimated annual range of 0.02–13.6 t ha^{-1} and 0.05–32 t ha^{-1}, respectively. On the other hand, the RUSLE simulated lower values compared to the average soil loss rate of 11 t/ha/yr, as reported by Borelli et al. [129] in the Apennines. Apart from mean soil loss, RUSLE also yielded a higher peak value than PESERA, a fact consistent with the literature findings [18,24,123,130]. This was attributed to the different character of the model and the way they approach the soil erosion mechanism, i.e., RUSLE is an empirical model developed to estimate annual soil loss in croplands [10], while PESERA is a runoff-based model developed to quantify water erosion [14]. Overall, the models do not account for gully, bank, and channel erosion, so any of these processes are excluded from the erosion rates. This difference between the simulations and the actual UAV- measurements may be partly attributed to the lack of gully erosion estimation from the models. Panagos et al. [131] highlight that the mean erosion values calculated by the national institutes (EIONET-SOIL) are greater than the PESERA rates, so as also reported in our case, there is an underestimation prediction of the model for this Mediterranean mountainous small-size watershed, where no agricultural land is present.

The sediment transport (at the watershed outlet) limitation of RUSLE and PESERA was surpassed by utilizing the IC and SDR indices. In our study, the SDR equations tested showed similar results; hence a mean value was applied. Our approach is in accordance with other similar approximations found in the literature [21,36,101,132–135]. The rate differences could be attributed to SDR underestimation (calculated value 40%) where uncertainties occur. Hence, a further sensitivity analysis led to the acceptance of this value based on multiple equation implementation and literature review. Every equation applied led to a 35–45% value range, including an additional SDR estimation based on the main stream length and mean basin CN (based on Williams equation, 1977 [136]), which resulted in a value of 46% SDR (CN = 65 for total watershed according to USDA soil Hydrologic group and land use), so the mean value of 40% is considered to be appropriate for this type of Mediterranean watershed.

Overall, Remote sensing and UAV-SfM techniques can support quantitively and in cm-scale the monitoring of soil erosion and deposition. This methodology offers the capability of actual cm-accuracy measurements in complex catchments where no vegetation cover (or where it is removed) is present, and the deposition rate is higher when compared to the measurement error estimation. This type of cm-surface reconstruction in complex environments leads to a cm-accurate pathway and spatial sediment volume distribution delineation. As a result, the annual stream pathway changes and redistribution pattern leads to an accurate sediment volume estimation, where sediment removal and dam management practices need to be applied. Furthermore, reservoirs of sediment retention dams are seldom resurveyed in the years following their construction, and their initial volume estimates are limited by the accuracy of the topographic maps used. Hence, such surveys are of utmost importance to engineers and stakeholders to assess (i) the life expectancy and current storage capacity of the dam, (ii) its operational and maintenance cost (e.g., dead volume storage restoration), and (iii) the necessity of taking erosion control measures, [137,138] aiming to serve as a framework guide application for similar cases/study sites.

5. Conclusions

This study uses new advances in remote sensing and UAV photogrammetry for measuring with high accuracy (cm scale) the annual sediment yield deposited on a retention dam in a small (870 ha) Mediterranean-type watershed. The methodology proposed in this study can be used as guidance for high-accuracy sediment yield deposition measurement through the detailed analysis of 3D modeling and point cloud comparison related to the high density of the UAV-SfM data collection. The UAV-SfM emerging technique appears to accurately measure topsoil change detection and erosion/deposition patterns, and the derived point clouds adequately simulated the upland dam basin topsoil microtopography. The annual sediment transport and the sediment pathways were accurately delineated due

to the cm-based surface reconstruction. Additionally, the annual monitoring of sediment yield is feasible through the cost-effective technique of UAV-SfM.

The 3D point-to-point comparison and the M_3C_2 distance algorithm are suitable for annual (September 2020 to August 2021 and October 2021 to September 2022) sediment quantification, delivering a mean sediment yield of about 1620 m^3 or 6.05 t ha^{-1} yr^{-1} and 3500 m^3 or 13 t ha^{-1} yr^{-1} for 2020–2021 and 2021–2022 estimation. The errors extracted correspond to the order of a few centimeters (2–3 cm), while point cloud analysis can be successively applied to swiftly changing landscapes, such as erosion-prone areas, in conjunction with the phenomenon's temporal evolution. Overall, the UAVs constitute a valuable, cost-effective tool for rapid assessment of soil degradation and topsoil change detection.

Additionally, the monitoring of the sediment deposition offers the possibility to evaluate two of the most widely used soil erosion models in Europe, the PESERA and the RUSLE. Both models seem to underestimate erosion rates in the Platana catchment, with RUSLE yielding higher soil loss rates compared to PESERA, against the field measurements, even though gully, bank and channel erosion are not considered. The PESERA and RUSLE models estimated a 2020–2021 annual mean gross erosion at 1.12 t ha^{-1} yr^{-1} and 3.51 t ha^{-1} yr^{-1}, respectively, while a significant increase was recorded at the 2021–2022 simulation (2.49 t ha^{-1} yr^{-1} and 3.56 t ha^{-1} yr^{-1}, respectively).

Overall, the study can serve as a reference guide on high-accuracy sediment yield measurements, especially in complex mountainous catchments, providing an indirect estimate of erosion rate estimations and offering a realistic assessment of the retention dams' life expectancy that could be crucial for the mitigation of flooding events and debris flows to nearby villages.

Author Contributions: Conceptualization, S.A. and I.P.; methodology, S.A., M.K., N.E. and I.P.; software, S.A. and E.P.; validation, S.A. and I.P.; fieldwork, S.A.; writing—original draft preparation, S.A., N.E., M.K., E.P. and N.C.; supervision, I.P. All authors have read and agreed to the published version of the manuscript.

Funding: This research is co-financed by Greece and the European Union (European Social Fund-ESF) through the Operational Programme «Human Resources Development, Education and Lifelong Learning» in the context of the project "Strengthening Human Resources Research Potential via Doctorate Research—2nd Cycle" (MIS-5000432), implemented by the State Scholarships Foundation (ΙΚΥ).

Acknowledgments: The authors would like to thank the Greek Control Agency for Guidance and Guarantee Community Aid (PCAGGCA) for providing the relevant land cover map, the National Observatory of Athens for providing the meteorological data of Makrakomi station). Additionally, we thank Tobia Lakes (Humboldt-Universität zu Berlin) for her fruitful comments regarding an earlier version of the manuscript.

Conflicts of Interest: The authors declare no conflict of interest.

Appendix A. The PESERA Application

The climate-related parameters were calculated based on local meteorological station records operated by the National Observatory of Athens (Makrakomi NOANN weather station) [139], and the topography-related parameters were derived from the DEM 5 × 5 m. The land use parameter registration was based on the validated CLC 2018 dataset, while the monthly vegetation cover was estimated using the Fraction of Vegetation Cover (FVC) [93]. NDVI, the component of Equation (1), was used for the estimation of the vegetation coverage percentage. The complete NDVI time series 2005–2021 was assessed via Google Earth Engine (Figure A1). The basin consists of continuous vegetation cover (annual mean value greater than 60%), and no wildfire event has occurred at least over the last 18 years.

Table A1. PESERA soil classes.

Soil Samples	Texture Code	Texture
Alluvial deposits	L	2
Calcareous soils	SL	1
Volcanic soils	CL	2

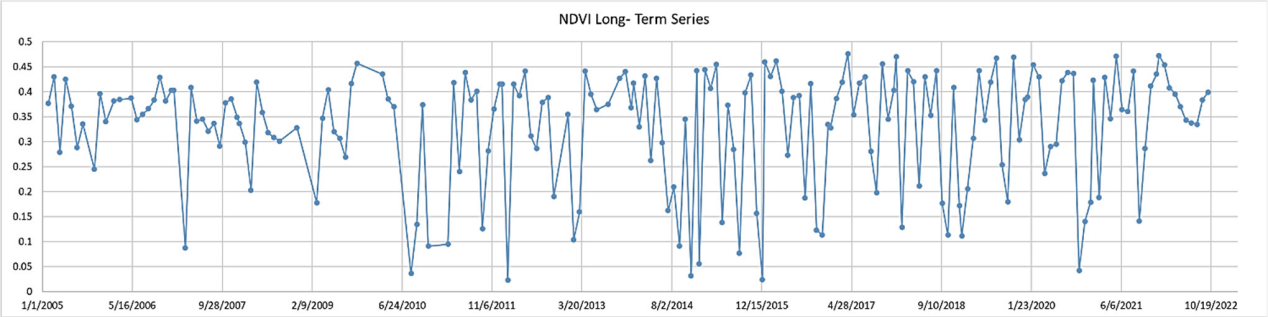

Figure A1. NDVI timeseries 2005–2022 (Google Earth Engine processed).

The soil dataset includes the susceptibility to surface crusting and erosion, the effective soil water storage capacity (SWSC), the soil water available to plants (AWSC at topsoil and subsoil), and the scale depth for erosion assessment (zm). For the evaluation of these parameters, an in-depth analysis of various physical–chemical soil characteristics is required [140]. The Soil Texture (ST) and the organic matter content (OMC) were specified through laboratory analysis for the demarcated soil mapping units. The Parent Material (PM) and the type of soil were specified using the available maps (1997 Ministry of Rural Development and Food (1:50,000) and the 1:30,000 Misopilinos 2015 AUTH Lamia's soil map), and they were validated by in situ inspection in August 2020. The susceptibility to surface crusting and erosion were approximated based on recorded soil characteristics (ST and OMC), the dominant land use type of the Soil Mapping Unit (SMU) and Table A2 provided by le Bissonnais et al. [140].

Table A2. Assessment of soil crusting and soil erodibility by the combination of physical–chemical and textural crusting parameters and textural erodibility parameters, respectively [140].

Physical Chemical Erodibility Textural Crusting	1 Very Low	2 Low	3 Medium	4 High	5 Very High
1 very low	1	1	1	2	3
2 low	1	2	2	3	5
3 medium	2	2	3	4	5
4 high	2	3	4	4	5
5 very high	3	4	5	5	5
Physical Chemical Erodibility Textural Erodibility					
1 very low	1	1	1	2	3
2 low	2	2	2	3	4
3 medium	3	3	3	4	5
4 high	3	4	4	4	5
5 very high	4	4	5	5	5

The concluded crusting and erodibility classes were translated into suitable values for the PESERA model based on the proposed values in Table A3 [29].

Table A3. Erodibility and crusting proposed values [29].

Proposed Values		
Class	**Erodibility**	**Crusting**
1	0.1	100
2	1	20
3	3	10
4	6	5
5	12	2

The Soil Water Storage Capacity (SWSC) is a soil property that can be approached in a multitude of ways. Richards [141] distinguished two main contributing processes: (a) the ability of plant roots to absorb and use the water and (b) the speed with which water can move inside the soil body in order to refill the water consumed by the plants. da Silva et al. [142] introduced the concept of least limiting water range (LLWR), which goes beyond the definition of Available Water Capacity (AWC). LLWR was defined as the range of water content within which limitations for plant growth associated with the water potential, aeration, and mechanical resistance are minimal.

Other factors based on which the SWSC has been estimated are the Bulk Density, the Packing Density, the Relative Field Capacity, the Air Capacity, the microporosity, the structural stability, the degree of compactness, etc. [143]. The current study estimates the SWSC of Soil Typological Units (STU), as indicated by [13]. The required input and the assumptions conducted for the calculation of the SWSC are presented in Table A4.

Table A4. The PESERA model SWSC implementation.

Parameter	Symbol	Value	Class	Assumption
Depth to rock	Dr	40–80 cm	M	This range of values covers all STUs
Depth restriction	Dr_rest Dr_res_10t	60 cm	M	Given that Dr_rest < 200 cm, Dr_rest = Dr_res_10t
Obstacle to roots	Roo	40–60 cm	3	This range of values covers all STUs
Topsoil/subsoil Packing Density	Pd_top Pd_sub	1.4 g/cm^3 (Lower value)	L	Laboratory analysis measured for all samples OM < 3% *1
Texture of top/subsoil	Textawctop Textawcsub	Coarse Medium	1 2	*1 The texture of the soil samples was within the ranges Clay < 18% & Sand > 65% Clay < 18% & 15% < Sand < 65% and
Available water capacity in top- & subsoil	AWC_top2s/2 mm AWC_sub2s/2 mm	120 mm/m 220 mm/m	Medium Very High	*1
Drainable pores in topsoil	Po_top %	30 20		Coarse textured soil Medium-textured soil
Drainable pores in subsoil	Po_sub %	25 18		Coarse textured soil Medium-textured soil
Portion of SWAP in top- & subsoil	P1swap_top/sub	1		For both the coarse and medium—textured soil
	SWSC_eff	154.5 mm 189 mm		Coarse textured soil Medium-textured soil

*1: The soil is treated as a uniform body. No clear distinction between top and sub-soil was recorded; L: Low; M: Moderate.

The scale depth parameter (zm) is a constant assuming a homogeneous subsurface hydraulic behavior of soil, which depends on soil texture [144]. It derives from the TOPMODEL, a set of conceptual models intended to describe hydrological processes, typically at the catchment level and in humid environments [145]. The correspondence between soil texture and the zm, as indicated by Kirkby et al. [13], is applied in the current work (Table A5).

Table A5. PESERA zm estimation according to soil texture class [13].

Soil Texture	Code	zm (mm)
Coarse	C	30
Fine	F	10
Medium	M	20
Medium fine	MF	15
Organic soils	O	10
Very fine	VF	5

The initial surface roughness and the surface roughness reduction per month are parameters specified based on the vegetation cover type and introduced into the model based on Gobin & Govers [29] (Table A6).

Table A6. PESERA zm estimation according to soil texture class [29].

Land Cover Type	Initial Roughness Storage (Rough 0 mm)	% Reduction after 1 Month
Both (in 1 year) arable	10	50
Cereal-dry farmed	10	50
Natural degraded	5	0
Forest (close canopy)	5	0
Heterogeneous	5	0
Permanent pasture	5	0
Rock, urban, wetlands etc	0	0
Spring sown arable	10	50
Vineyards, tree crops etc	5	0
Autumn sown Med'n arable	10	50
Winter sown arable	10	50
Uncultivated-natural vegetation	5	0
Bare ground	5	0

The climate parameters were calculated based on the meteorological data acquired by the National Observatory of Athens weather station of Makrakomi covering three periods: 2020, 2021, and 2022. From October 2022 to December 2022, meteorological values were set to zero. The climatic data comprises daily time series of rainfall, temperature, and potential evapotranspiration. The data were interpolated to a 5 m pixel size raster. These data were used to provide the monthly data layers required. The required data include mean monthly rainfall, mean monthly rainfall per rain day, coefficient of variation of monthly rainfall, mean monthly temperature and monthly temperature range (max–min). Mean monthly PET values were calculated using the FAO ETo calculator, with monthly input data for mean, min and max Temperature, RH, wind speed, and location characteristics. The FAO ETo calculator estimates evapotranspiration based on the FAO Penman–Monteith

equation [146]. Finally, the topographic data include the standard deviation of the elevation layer, which was calculated based on DEM (5 × 5 m pixel size) in the ArcGIS environment. (v. 10.5, Environmental Systems Research Institute-ESRI, Redlands, CA, USA). Table A7 presents all input parameters with their data source.

Table A7. PESERA zm estimation according to soil texture class.

Model Parameter	Value Range	Input Data Description/Reference
Land cover type (use)	240, 320	CORINE 2018, processed by fieldwork
Coverage	0–100%	Based on FVC and NDVI computed on Google Earth Engine
Surface roughness reduction (roughed)	0.1	[29]
Surface roughness (rough0)	5	[29]
Root depth	400, 600 mm	[29]
Surface crusting	20, 40	[29]
Soil erodibility	2	[29]
Effective Soil Water Storage Capacity (SWSC)	154.5–189 mm	[13]
zm	20, 30 (mm)	[13]
Meteorological data	Value range based on meteorological data (mm) analysis	Processed by the researchers FAO Penman–Monteith equation. (FAO ETo calculator)
Standard deviation of elevation	0–10.01	Processed by ArcGIS

Appendix B. The RUSLE Application

The R-factor was estimated based on the rainfall erosivity index EI30 (MJ mm ha^{-1} h^{-1}) [147] (Table A8, Figure A2a,b), using the RIST (Rainfall Intensity Summarization Tool) platform [148]. Low-intensity rain events, i.e., with precipitation values less than 12.7 mm (in 10 min step), were excluded from the energy and intensity calculations since they have a minor effect on EI30.

The K-factor (Figure A2c) was calculated based on the fieldwork performed at the basin. Specifically, three distinct lithological units were identified, namely calcareous rocks (dolomites and limestones), alluvial deposits, and volcanic formations. Such description is necessary due to the decisive effect of the underlying bedrock on runoff and sedimentation potential and the fact that soil erodibility can easily be related to the bedrock's susceptibility to erosion [149]. Hence, the soil formations developed per unit were recorded, and an erodibility value was assigned to each (Table A9), calculated based on the equation of Wischmeier and Smith [7]. Given the relatively small size of the basin, and the fact that clay loam soils occupy their larger part (i.e., soil variability is rather small), spatial interpolation was not performed, and a static K-factor value was assigned to each formation instead. The coefficient values ranged between 0.016 and 0.022 t ha h ha^{-1} MJ^{-1} mm^{-1}, with a mean (spatial) value of 0.021 t ha h ha^{-1} MJ^{-1} mm^{-1}. The highest K values characterize the most erosion-prone formations (e.g., volcanic formations), while the lowest are the most resistant ones (e.g., limestones).

The composite LS-factor (Figure A2d) was based on the local 5 m DEM, developed especially for the needs of the study. Calculations were made on the SAGA GIS software package provided by QGIS, employing the Desmet and Govers [150] equation.

The C-factor (Figure A2e) was calculated based on the basin's Land use/Land Cover (LULC) delineation (Table 4). Three distinct level-1 classes were identified, namely Agricultural areas, Forest, and semi-natural areas. A cover management coefficient value was assigned, following the methodology presented in Efthimiou et al. [91], an adjusted ap-

proximation of the work of Panagos et al. [30] that aims to incorporate and exploit the spatiotemporal dynamics of land use and the intra-annual variability of vegetation characteristics. In brief, the LULC map was divided into arable/non-arable land and non-erodible uses (e.g., Artificial areas, etc.). Arable lands and non-erodible uses were assigned with a non-temporal C-factor value considering a bibliographic review [7,30,42,43]. In non-arable lands, the parameter was estimated utilizing Equation (9), according to which the C-factor is a function of its empirical bibliographic value range per feature class, adjusted to the spatiotemporal variation of vegetation cover. The latter was assessed employing a proxy vegetation layer (Fcover) at 10 m resolution, developed from Sentinel-2 imagery and literature data on crop types. The lowest values characterize densely vegetated areas (e.g., non-arable land), and the highest areas of mild or low vegetation cover (e.g., arable land). The P-factor (Figure A2f) was set equal to the unit since no support practices take place in the study area.

$$C_{NonArable} = Min(C_{landuse}) + Range(C_{landuse}) \times (1 - F_{cover}), \quad (9)$$

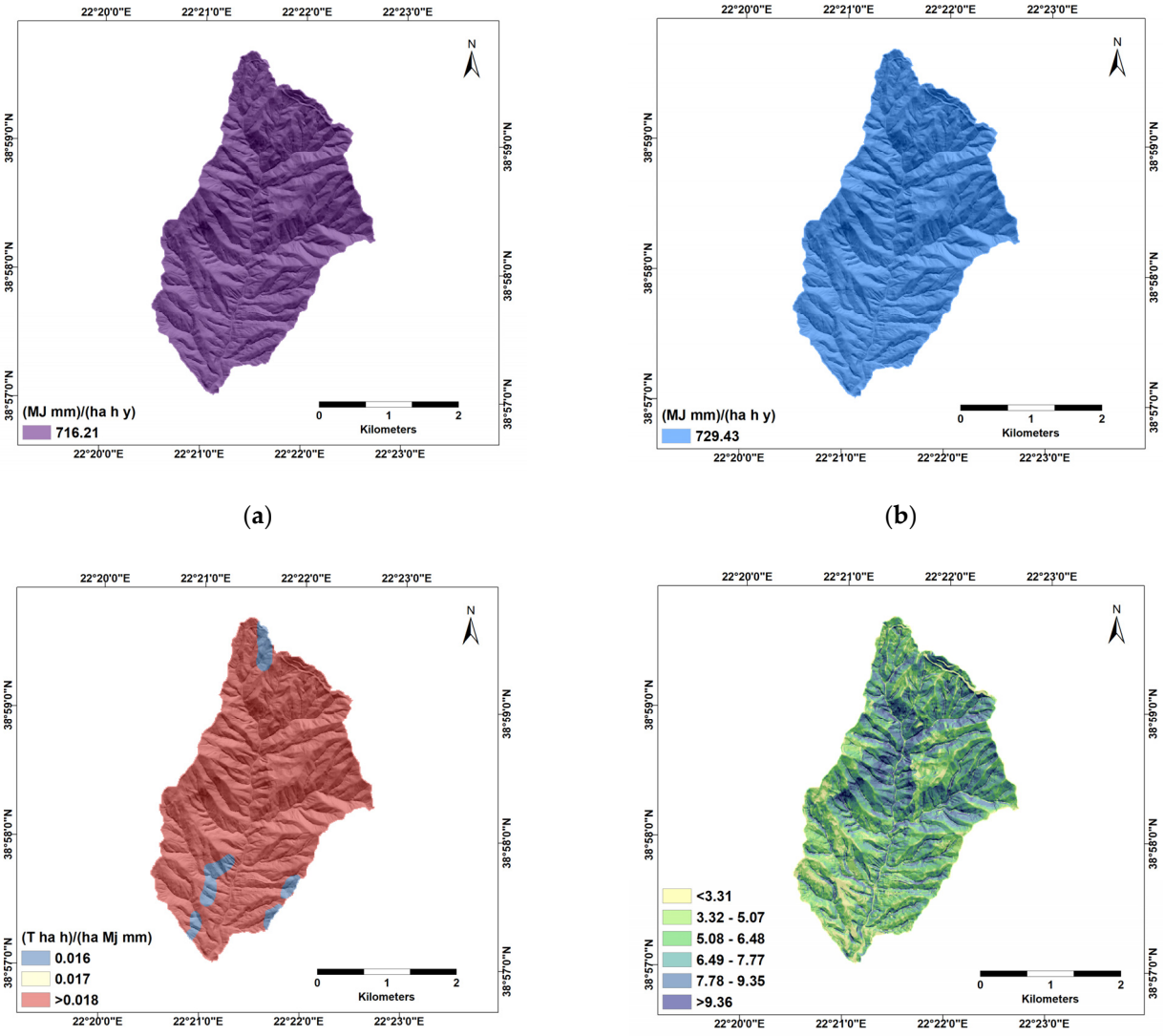

Figure A2. *Cont.*

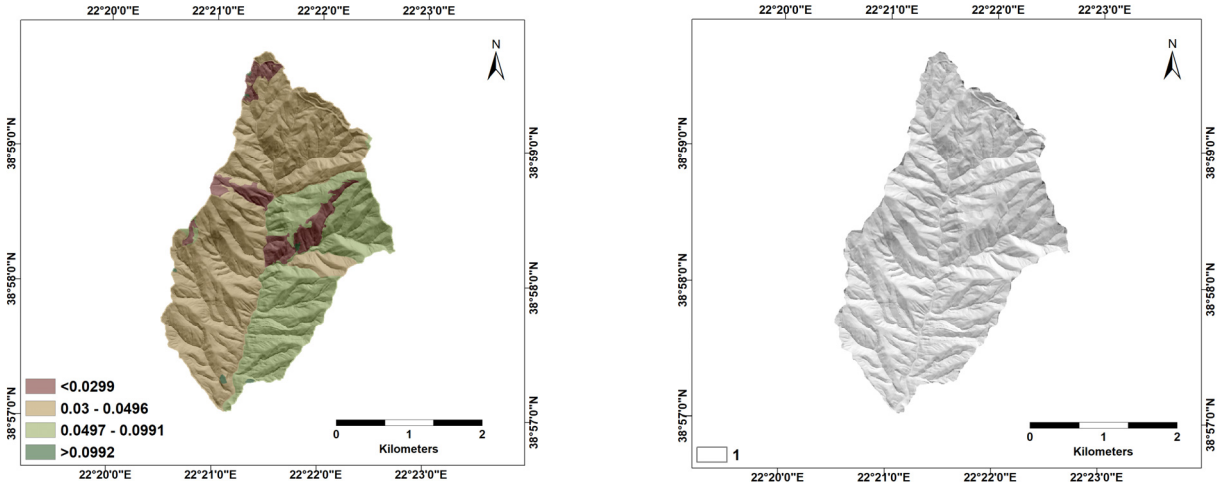

(**e**) (**f**)

Figure A2. The RUSLE application. (**a**) R-factor 2020–2021; (**b**) R-factor 2021–2022; (**c**) K-factor; (**d**) LS-factor; (**e**) C-factor; (**f**) P-factor.

Table A8. R-factor values, analytical estimation, Makrakomi station, September 2020–August 2021/October 2021–September 2022.

	Rain [1] (mm)	Rain [2] (mm)	Energy (MJ ha^{-1})	EI_{30} (MJ mm ha^{-1} h^{-1})	Erosivity Density * (MJ ha^{-1} h^{-1})
TOTAL * 2020–2021	572.00	490.91	44.46	716.21	1.46
TOTAL * 2021–2022	793.20	599.15	74.31	729.43	1.22

[1] Precipitation measurements—all storms included; [2] Precipitation data—RIST outputs after storm exclusions; * Total values represent the sum of monthly averages, except for Erosivity Density, which is the ratio of total EI30 to total precipitation.

Table A9. Soil attributes of the Platana Dam basin and K-factor values.

Soil Samples (Texture)	K-Factor
Sandy Loam (SL) soil	0.016
Clay Loam (CL) soil	0.022
Loam (L)	0.017

References

1. Dregne, H.E. Land degradation in the drylands. *Arid L. Res. Manag.* **2002**, *16*, 99–132. [CrossRef]
2. Gao, P.; Pasternack, G.B.; Bali, K.M.; Wallender, W.W. Suspended-sediment transport in an intensively cultivated watershed in southeastern California. *Catena* **2007**, *69*, 239–252. [CrossRef]
3. Carrivick, J.L.; Smith, M.W.; Quincey, D.J. *Structure from Motion in the Geosciences*; John Wiley & Sons: Hoboken, NJ, USA, 2016; pp. 1–8. [CrossRef]
4. De Roo, A.P.J.; Hazelhoff, L.; Burrough, P.A. Soil erosion modelling using 'answers' and geographical information systems. *Earth Surf. Process. Landf.* **1989**, *14*, 517–532. [CrossRef]
5. Karydas, C.G.; Panagos, P.; Gitas, I.Z. A classification of water erosion models according to their geospatial characteristics. *Int. J. Digit. Earth* **2014**, *7*, 229–250. [CrossRef]
6. Mitra, B.; Scott, H.D.; Dixon, J.C.; McKimmey, J.M. Applications of fuzzy logic to the prediction of soil erosion in a large watershed. *Geoderma* **1998**, *86*, 183–209. [CrossRef]
7. Wischmeier, W.H.; Smith, D.D.; Science and Education Administration, U.S. Department of Agriculture. *Predicting Rainfall Erosion Losses: A Guide to Conservation Planning*; USDA Publications, Ed.; Science and Education Administration, U.S. Department of Agriculture: Washington, DC, USA, 1978.

8. Gavrilovic, Z. The Use of an Empirical Method for Calculating Sediment Production and Transport in Unsuited or Torrential Streams. In *Proceedings of the International Conference for Review Regime*; Scientific Research Publishing, Ed.; Scientific Research Publishing: Wallingford, UK, 1988; pp. 411–422.
9. Renard, K.; Foster, G.R.; Weesies, G.; Mccool, D.; Yoder, D. *Predicting Soil Erosion by Water: A Guide to Conservation Planning with the Revised Universal Soil Loss Equation (RUSLE)*; United States Government Printing: Washington, DC, USA, 1997.
10. Renard, K.G.; Foster, G.R.; Weesies, G.A.; Porter, J.P. RUSLE: Revised universal soil loss equation. *J. Soil Water Conserv.* **1991**, *46*, 30–33.
11. Laflen, J.M.; Lane, L.J.; Foster, G.R. WEPP: A new generation of erosion prediction technology. *J. Soil Water Conserv.* **1991**, *46*, 34–38.
12. Neitsch, S.L.; Arnold, J.G.; Kiniry, J.R.; Williams, J.R. *Soil and Water Assessment Tool Theoretical Documentation*; Texas Water Resources Institute, Ed.; Scientific Research Publishing: Wallingford, UK, 2005.
13. Kirkby, M.J.; Irvine, B.J.; Jones, R.J.A.; Govers, G. The PESERA coarse scale erosion model for Europe. I.—Model rationale and implementation. *Eur. J. Soil Sci.* **2008**, *59*, 1293–1306. [CrossRef]
14. Kirkby, M.J.; Jones, R.J.A.; Irvine, B.; Gobin, A.; Govers, G.; Cerdan, O.; van Rompaey, A.J.J.; le Bissonnais, Y.; Daroussin, J.; King, D.; et al. *Pan-European Soil Erosion Risk Assessment: The PESERA Map*. 2003. Available online: https://www.researchgate.net/publication/265357850_Pan-European_soil_erosion_risk_assessment_the_PESERA_Map_Version_1_October_2003#fullTextFileContent (accessed on 1 September 2022).
15. Karydas, C.G.; Panagos, P. The G2 erosion model: An algorithm for month-time step assessments. *Environ. Res.* **2018**, *161*, 256–267. [CrossRef]
16. Li, P.; Zang, Y.; Ma, D.; Yao, W.; Holden, J.; Irvine, B.; Zhao, G. Soil erosion rates assessed by RUSLE and PESERA for a Chinese Loess Plateau catchment under land-cover changes. *Earth Surf. Process. Landf.* **2020**, *45*, 707–722. [CrossRef]
17. Kaffas, K.; Pisinaras, V.; Al Sayah, M.J.; Santopietro, S.; Righetti, M. A USLE-based model with modified LS-factor combined with sediment delivery module for Alpine basins. *Catena* **2021**, *207*, 105655. [CrossRef]
18. Karamesouti, M.; Petropoulos, G.P.; Papanikolaou, I.D.; Kairis, O.; Kosmas, K. Erosion rate predictions from PESERA and RUSLE at a Mediterranean site before and after a wildfire: Comparison & implications. *Geoderma* **2016**, *261*, 44–58. [CrossRef]
19. Tsara, M.; Kosmas, C.; Kirkby, M.J.; Kosma, D.; Yassoglou, N. An evaluation of the pesera soil erosion model and its application to a case study in Zakynthos, Greece. *Soil Use Manag.* **2005**, *21*, 377–385. [CrossRef]
20. Kinnell, P.I.A. Event soil loss, runoff and the Universal Soil Loss Equation family of models: A review. *J. Hydrol.* **2010**, *385*, 384–397. [CrossRef]
21. De Vente, J.; Poesen, J.; Verstraeten, G.; Govers, G.; Vanmaercke, M.; Van Rompaey, A.; Arabkhedri, M.; Boix-Fayos, C. Predicting soil erosion and sediment yield at regional scales: Where do we stand? *Earth-Sci. Rev.* **2013**, *127*, 16–29. [CrossRef]
22. Esteves, T.C.J.; Kirkby, M.J.; Shakesby, R.A.; Ferreira, A.J.D.; Soares, J.A.A.; Irvine, B.J.; Ferreira, C.S.S.; Coelho, C.O.A.; Bento, C.P.M.; Carreiras, M.A. Mitigating land degradation caused by wildfire: Application of the PESERA model to fire-affected sites in central Portugal. *Geoderma* **2012**, *191*, 40–50. [CrossRef]
23. Vieira, D.C.S.; Malvar, M.C.; Martins, M.A.S.; Serpa, D.; Keizer, J.J. Key factors controlling the post-fire hydrological and erosive response at micro-plot scale in a recently burned Mediterranean forest. *Geomorphology* **2018**, *319*, 161–173. [CrossRef]
24. Fernández, C.; Vega, J.A. Evaluation of RUSLE and PESERA models for predicting soil erosion losses in the first year after wildfire in NW Spain. *Geoderma* **2016**, *273*, 64–72. [CrossRef]
25. Anderson, K.; Ryan, B.; Sonntag, W.; Kavvada, A.; Friedl, L. Earth observation in service of the 2030 Agenda for Sustainable Development. *Geo-Spat. Inf. Sci.* **2017**, *20*, 77–96. [CrossRef]
26. Batista, P.V.G.; Davies, J.; Silva, M.L.N.; Quinton, J.N. On the evaluation of soil erosion models: Are we doing enough? *Earth-Sci. Rev.* **2019**, *197*, 102898. [CrossRef]
27. Alewell, C.; Borrelli, P.; Meusburger, K.; Panagos, P. Using the USLE: Chances, challenges and limitations of soil erosion modelling. *Int. Soil Water Conserv. Res.* **2019**, *7*, 203–225. [CrossRef]
28. Van Rompaey, A.J.; Vieillefont, V.; Jones, R.J.; Montanarella, L.; Verstraeten, G.; Bazzoffi, P.; Dostal, T.; Krasa, J.; de Vente, J.; Poesen, J. *Pan-European Soil Erosion Risk Assessment Deliverable 7B: Model Validation at the Catchment Scale*. 2003. Available online: https://esdac.jrc.ec.europa.eu/ESDB_Archive/pesera/pesera_cd/pdf/DL7BValidationCatchment.pdf (accessed on 1 September 2022).
29. Gobin, A.; Govers, G. *Pan-European Soil Erosion Risk Assessment Project. Second Annual Report to the European Commission. EC Contract No. QLK5-CT-1999-01323*; EU: Brussels, Belgium, 2002.
30. Panagos, P.; Borrelli, P.; Meusburger, K.; Alewell, C.; Lugato, E.; Montanarella, L. Estimating the soil erosion cover-management factor at the European scale. *Land Use Policy* **2015**, *48*, 38–50. [CrossRef]
31. Polykretis, C.; Alexakis, D.D.; Grillakis, M.G.; Manoudakis, S. Assessment of Intra-Annual and Inter-Annual Variabilities of Soil Erosion in Crete Island (Greece) by Incorporating the Dynamic "Nature" of R and C-Factors in RUSLE Modeling. *Remote Sens.* **2020**, *12*, 2439. [CrossRef]
32. Sigalos, G.; Loukaidi, V.; Dasaklis, S.; Drakopoulou, P.; Salvati, L.; Ruiz, P.S.; Mavrakis, A. Soil erosion and degradation in a rapidly expanding industrial area of Eastern Mediterranean basin (Thriasio plain, Greece). *Nat. Hazards J. Int. Soc. Prev. Mitig. Nat. Hazards* **2016**, *82*, 2187–2200. [CrossRef]

33. Efthimiou, N.; Lykoudi, E.; Karavitis, C. Comparative analysis of sediment yield estimations using different empirical soil erosion models. *Hydrol. Sci. J.* **2017**, *62*, 2674–2694. [CrossRef]
34. Rozos, D.; Skilodimou, H.D.; Loupasakis, C.; Bathrellos, G.D. Application of the revised universal soil loss equation model on landslide prevention. An example from N. Euboea (Evia) Island, Greece. *Environ. Earth Sci.* **2013**, *70*, 3255–3266. [CrossRef]
35. Walling, D.E. The sediment delivery problem. *J. Hydrol.* **1983**, *65*, 209–237. [CrossRef]
36. Borselli, L.; Cassi, P.; Torri, D. Prolegomena to sediment and flow connectivity in the landscape: A GIS and field numerical assessment. *Catena* **2008**, *75*, 268–277. [CrossRef]
37. Cavalli, M.; Trevisani, S.; Comiti, F.; Marchi, L. Geomorphometric assessment of spatial sediment connectivity in small Alpine catchments. *Geomorphology* **2013**, *188*, 31–41. [CrossRef]
38. Aucelli, P.P.C.; Conforti, M.; Della Seta, M.; Del Monte, M.; D'uva, L.; Rosskopf, C.M.; Vergari, F. Multi-temporal Digital Photogrammetric Analysis for Quantitative Assessment of Soil Erosion Rates in the Landola Catchment of the Upper Orcia Valley (Tuscany, Italy). *L. Degrad. Dev.* **2016**, *27*, 1075–1092. [CrossRef]
39. De Jong, S.M. Derivation of vegetative variables from a landsat tm image for modelling soil erosion. *Earth Surf. Process. Landforms* **1994**, *19*, 165–178. [CrossRef]
40. Meusburger, K.; Bänninger, D.; Alewell, C. Estimating vegetation parameter for soil erosion assessment in an alpine catchment by means of QuickBird imagery. *Int. J. Appl. Earth Obs. Geoinf.* **2010**, *12*, 201–207. [CrossRef]
41. Wang, R.; Zhang, S.; Pu, L.; Yang, J.; Yang, C.; Chen, J.; Guan, C.; Wang, Q.; Chen, D.; Fu, B.; et al. Gully Erosion Mapping and Monitoring at Multiple Scales Based on Multi-Source Remote Sensing Data of the Sancha River Catchment, Northeast China. *ISPRS Int. J. Geo-Inf.* **2016**, *5*, 200. [CrossRef]
42. Efthimiou, N.; Psomiadis, E. The Significance of Land Cover Delineation on Soil Erosion Assessment. *Environ. Manag.* **2018**, *62*, 383–402. [CrossRef]
43. Efthimiou, N.; Psomiadis, E.; Panagos, P. Fire severity and soil erosion susceptibility mapping using multi-temporal Earth Observation data: The case of Mati fatal wildfire in Eastern Attica, Greece. *Catena* **2020**, *187*, 104320. [CrossRef]
44. Alexiou, S.; Deligiannakis, G.; Pallikarakis, A.; Papanikolaou, I.; Psomiadis, E.; Reicherter, K. Comparing High Accuracy t-LiDAR and UAV-SfM Derived Point Clouds for Geomorphological Change Detection. *ISPRS Int. J. Geo-Inf.* **2021**, *10*, 367. [CrossRef]
45. Deligiannakis, G.; Pallikarakis, A.; Papanikolaou, I.; Alexiou, S.; Reicherter, K. Detecting and Monitoring Early Post-Fire Sliding Phenomena Using UAV–SfM Photogrammetry and t-LiDAR-Derived Point Clouds. *Fire* **2021**, *4*, 87. [CrossRef]
46. Kociuba, W.; Janicki, G.; Rodzik, J.; Stępniewski, K. Comparison of volumetric and remote sensing methods (TLS) for assessing the development of a permanent forested loess gully. *Nat. Hazards J. Int. Soc. Prev. Mitig. Nat. Hazards* **2015**, *79*, 139–158. [CrossRef]
47. Longoni, L.; Papini, M.; Brambilla, D.; Barazzetti, L.; Roncoroni, F.; Scaioni, M.; Ivanov, V.I. Monitoring Riverbank Erosion in Mountain Catchments Using Terrestrial Laser Scanning. *Remote Sens.* **2016**, *8*, 241. [CrossRef]
48. D'Oleire-Oltmanns, S.; Marzolff, I.; Peter, K.D.; Ries, J.B. Unmanned Aerial Vehicle (UAV) for Monitoring Soil Erosion in Morocco. *Remote Sens.* **2012**, *4*, 3390–3416. [CrossRef]
49. Eltner, A.; Baumgart, P.; Maas, H.G.; Faust, D. Multi-temporal UAV data for automatic measurement of rill and interrill erosion on loess soil. *Earth Surf. Process. Landf.* **2015**, *40*, 741–755. [CrossRef]
50. Neugirg, F.; Stark, M.; Kaiser, A.; Vlacilova, M.; Della Seta, M.; Vergari, F.; Schmidt, J.; Becht, M.; Haas, F. Erosion processes in calanchi in the Upper Orcia Valley, Southern Tuscany, Italy based on multitemporal high-resolution terrestrial LiDAR and UAV surveys. *Geomorphology* **2016**, *269*, 8–22. [CrossRef]
51. Li, P.; Hao, M.; Hu, J.; Gao, C.; Zhao, G.; Chan, F.K.S.; Gao, J.; Dang, T.; Mu, X. Spatiotemporal Patterns of Hillslope Erosion Investigated Based on Field Scouring Experiments and Terrestrial Laser Scanning. *Remote Sens.* **2021**, *13*, 1674. [CrossRef]
52. Bazzoffi, P. Measurement of rill erosion through a new UAV-GIS methodology. *Ital. J. Agron.* **2015**, *10*. [CrossRef]
53. Borrelli, L.; Conforti, M.; Mercuri, M. LiDAR and UAV System Data to Analyse Recent Morphological Changes of a Small Drainage Basin. *ISPRS Int. J. Geo-Inf.* **2019**, *8*, 536. [CrossRef]
54. Aber, J.; Marzolff, I.; Ries, J.; Aber, S. Small-Format Aerial Photography and UAS Imagery: Principles, Techniques and Geoscience Applications. In *Small-Format Aerial Photography and UAS Imagery*, 2nd ed.; Academic Press: Cambridge, MA, USA, 2019; pp. 1–382. [CrossRef]
55. Rieke-Zapp, D.H.; Nearing, M.A. Digital close range photogrammetry for measurement of soil erosion. *Photogramm. Rec.* **2005**, *20*, 69–87. [CrossRef]
56. Marzolff, I.; Poesen, J. The potential of 3D gully monitoring with GIS using high-resolution aerial photography and a digital photogrammetry system. *Geomorphology* **2009**, *111*, 48–60. [CrossRef]
57. Peter, K.D.; d'Oleire-Oltmanns, S.; Ries, J.B.; Marzolff, I.; Ait Hssaine, A. Soil erosion in gully catchments affected by land-levelling measures in the Souss Basin, Morocco, analysed by rainfall simulation and UAV remote sensing data. *Catena* **2014**, *113*, 24–40. [CrossRef]
58. Manfreda, S.; McCabe, M.F.; Miller, P.E.; Lucas, R.; Madrigal, V.P.; Mallinis, G.; Dor, E.B.; Helman, D.; Estes, L.; Ciraolo, G.; et al. On the Use of Unmanned Aerial Systems for Environmental Monitoring. *Remote Sens.* **2018**, *10*, 641. [CrossRef]
59. Yermolaev, O.; Usmanov, B.; Gafurov, A.; Poesen, J.; Vedeneeva, E.; Lisetskii, F.; Nicu, I.C. Assessment of Shoreline Transformation Rates and Landslide Monitoring on the Bank of Kuibyshev Reservoir (Russia) Using Multi-Source Data. *Remote Sens.* **2021**, *13*, 4214. [CrossRef]

60. Meinen, B.U.; Robinson, D.T. Mapping erosion and deposition in an agricultural landscape: Optimization of UAV image acquisition schemes for SfM-MVS. *Remote Sens. Environ.* **2020**, *239*, 111666. [CrossRef]
61. Cândido, B.M.; James, M.; Quinton, J.; de Lima, W.; Silva, M.L.N. Sediment source and volume of soil erosion in a gully system using UAV photogrammetry. *Rev. Bras. Ciência Solo* **2020**, *44*, e0200076. [CrossRef]
62. Cândido, B.M.; Quinton, J.N.; James, M.R.; Silva, M.L.N.; de Carvalho, T.S.; de Lima, W.; Beniaich, A.; Eltner, A. High-resolution monitoring of diffuse (sheet or interrill) erosion using structure-from-motion. *Geoderma* **2020**, *375*, 114477. [CrossRef]
63. Liu, K.; Ding, H.; Tang, G.; Na, J.; Huang, X.; Xue, Z.; Yang, X.; Li, F. Detection of Catchment-Scale Gully-Affected Areas Using Unmanned Aerial Vehicle (UAV) on the Chinese Loess Plateau. *ISPRS Int. J. Geo-Inf.* **2016**, *5*, 238. [CrossRef]
64. Harwin, S.; Lucieer, A. Assessing the Accuracy of Georeferenced Point Clouds Produced via Multi-View Stereopsis from Unmanned Aerial Vehicle (UAV) Imagery. *Remote Sens.* **2012**, *4*, 1573–1599. [CrossRef]
65. Westoby, M.J.; Brasington, J.; Glasser, N.F.; Hambrey, M.J.; Reynolds, J.M. 'Structure-from-Motion' photogrammetry: A low-cost, effective tool for geoscience applications. *Geomorphology* **2012**, *179*, 300–314. [CrossRef]
66. Pellicani, R.; Argentiero, I.; Manzari, P.; Spilotro, G.; Marzo, C.; Ermini, R.; Apollonio, C. UAV and Airborne LiDAR Data for Interpreting Kinematic Evolution of Landslide Movements: The Case Study of the Montescaglioso Landslide (Southern Italy). *Geosciences* **2019**, *9*, 248. [CrossRef]
67. Lucieer, A.; Turner, D.; King, D.H.; Robinson, S.A. Using an Unmanned Aerial Vehicle (UAV) to capture micro-topography of Antarctic moss beds. *Int. J. Appl. Earth Obs. Geoinf.* **2014**, *27*, 53–62. [CrossRef]
68. Padró, J.C.; Cardozo, J.; Montero, P.; Ruiz-Carulla, R.; Alcañiz, J.M.; Serra, D.; Carabassa, V. Drone-Based Identification of Erosive Processes in Open-Pit Mining Restored Areas. *Land* **2022**, *11*, 212. [CrossRef]
69. Pineux, N.; Lisein, J.; Swerts, G.; Bielders, C.L.; Lejeune, P.; Colinet, G.; Degré, A. Can DEM time series produced by UAV be used to quantify diffuse erosion in an agricultural watershed? *Geomorphology* **2017**, *280*, 122–136. [CrossRef]
70. Psomiadis, E.; Diakakis, M.; Soulis, K.X. Combining SAR and Optical Earth Observation with Hydraulic Simulation for Flood Mapping and Impact Assessment. *Remote Sens.* **2020**, *12*, 3980. [CrossRef]
71. Psomiadis, E. Long and Short-Term Coastal Changes Assessment Using Earth Observation Data and GIS Analysis: The Case of Sperchios River Delta. *ISPRS Int. J. Geo-Inf.* **2022**, *11*, 61. [CrossRef]
72. Psomiadis, E.; Parcharidis, I.; Stamatis, G.; Foumelis, M. Remotely sensing data and thematic mapping for sustainable developing in Sperchios river basin (Central Greece). *Remote Sens. Environ. Monit. GIS Appl. Geol. V* **2005**, *5983*, 408–419.
73. Psomiadis, E.; Charizopoulos, N.; Soulis, K.X.; Efthimiou, N. Investigating the Correlation of Tectonic and Morphometric Characteristics with the Hydrological Response in a Greek River Catchment Using Earth Observation and Geospatial Analysis Techniques. *Geosciences* **2020**, *10*, 377. [CrossRef]
74. Marinos, G.; Papastamatiou, J.; Maratos, G.; Melidonis, N.; Andronopoulos, B.; Tataris, A.; Betoulis, D.K.G.; Maragoudakis, N.; Lalechos, N. Geological Map of Greece, Lamia Sheet, Scale 1:50.000 1967.
75. Bouyoucos, G.J. Hydrometer Method Improved for Making Particle Size Analyses of Soils1. *Agron. J.* **1962**, *54*, 464–465. [CrossRef]
76. Walkley, A.J.; Black, I.A. Estimation of soil organic carbon by the chromic acid titration method. *Soil Sci.* **1934**, *37*, 29–38. [CrossRef]
77. Puliti, S.; Ørka, H.O.; Gobakken, T.; Næsset, E. Inventory of Small Forest Areas Using an Unmanned Aerial System. *Remote Sens.* **2015**, *7*, 9632–9654. [CrossRef]
78. Fraser, B.T.; Congalton, R.G. Issues in Unmanned Aerial Systems (UAS) Data Collection of Complex Forest Environments. *Remote Sens.* **2018**, *10*, 908. [CrossRef]
79. de Lima, R.S.; Lang, M.; Burnside, N.G.; Peciña, M.V.; Arumäe, T.; Laarmann, D.; Ward, R.D.; Vain, A.; Sepp, K. An Evaluation of the Effects of UAS Flight Parameters on Digital Aerial Photogrammetry Processing and Dense-Cloud Production Quality in a Scots Pine Forest. *Remote Sens.* **2021**, *13*, 1121. [CrossRef]
80. Tomaštík, J.; Mokroš, M.; Surový, P.; Grznárová, A.; Merganič, J. UAV RTK/PPK Method—An Optimal Solution for Mapping Inaccessible Forested Areas? *Remote Sens.* **2019**, *11*, 721. [CrossRef]
81. Sona, G.; Pinto, L.; Pagliari, D.; Passoni, D.; Gini, R. Experimental analysis of different software packages for orientation and digital surface modelling from UAV images. *Earth Sci. Inform.* **2014**, *7*, 97–107. [CrossRef]
82. Kaiser, A.; Neugirg, F.; Rock, G.; Müller, C.; Haas, F.; Ries, J.; Schmidt, J. Small-Scale Surface Reconstruction and Volume Calculation of Soil Erosion in Complex Moroccan Gully Morphology Using Structure from Motion. *Remote Sens.* **2014**, *6*, 7050–7080. [CrossRef]
83. Monserrat, O.; Crosetto, M. Deformation measurement using terrestrial laser scanning data and least squares 3D surface matching. *ISPRS J. Photogramm. Remote Sens.* **2008**, *63*, 142–154. [CrossRef]
84. Lague, D.; Brodu, N.; Leroux, J. Accurate 3D comparison of complex topography with terrestrial laser scanner: Application to the Rangitikei canyon (N-Z). *ISPRS J. Photogramm. Remote Sens.* **2013**, *82*, 10–26. [CrossRef]
85. Rouse, J.W.J.; Haas, R.H.; Schell, J.A.; Deering, D.W.; Haas, R.H.; Schell, J.A.; Deering, D.W. *Monitoring Vegetation Systems in the Great Plains with ERTS*; NASA Special Publications: Washington, DC, USA, 1974.
86. Niu, B.; Hong, S.; Yuan, J.; Peng, S.; Wang, Z.; Zhang, X. Global trends in sediment-related research in earth science during 1992–2011: A bibliometric analysis. *Scientometrics* **2014**, *98*, 511–529. [CrossRef]
87. Yang, X.; Yang, X. Deriving RUSLE cover factor from time-series fractional vegetation cover for hillslope erosion modelling in New South Wales. *Soil Res.* **2014**, *52*, 253–261. [CrossRef]

88. Sun, W.; Shao, Q.; Liu, J.; Zhai, J. Assessing the effects of land use and topography on soil erosion on the Loess Plateau in China. *Catena* **2014**, *121*, 151–163. [CrossRef]
89. Zhongming, W.; Lees, B.G.; Feng, J.; Wanning, L.; Haijing, S. Stratified vegetation cover index: A new way to assess vegetation impact on soil erosion. *Catena* **2010**, *83*, 87–93. [CrossRef]
90. Mikulicic, N.; Mihajlovic, Z. Procedural generation of mediterranean environments. In Proceedings of the 2016 39th International Convention on Information and Communication Technology, Electronics and Microelectronics (MIPRO), Opatija, Croatia, 30 May 2016–3 June 2016; pp. 261–266. [CrossRef]
91. Efthimiou, N.; Psomiadis, E.; Papanikolaou, I.; Soulis, K.X.; Borrelli, P.; Panagos, P. A new high resolution object-oriented approach to define the spatiotemporal dynamics of the cover-management factor in soil erosion modelling. *Catena* **2022**, *213*, 106149. [CrossRef]
92. Boettinger, J.L.; Ramsey, R.D.; Bodily, J.M.; Cole, N.J.; Kienast-Brown, S.; Nield, S.J.; Saunders, A.M.; Stum, A.K. Landsat spectral data for digital soil mapping. In *Digital Soil Mapping with Limited Data*; Springer: Dordrecht, The Netherlands, 2008; pp. 193–202. [CrossRef]
93. Zeng, X.; Dickinson, R.E.; Walker, A.; Shaikh, M.; Defries, R.S.; Qi, J.; Zeng, X.; Dickinson, R.E.; Walker, A.; Shaikh, M.; et al. Derivation and Evaluation of Global 1-km Fractional Vegetation Cover Data for Land Modeling. *JApMe* **2000**, *39*, 826–839. [CrossRef]
94. Gutman, G.; Ignatov, A. The derivation of the green vegetation fraction from NOAA/AVHRR data for use in numerical weather prediction models. *Int. J. Remote Sens.* **2010**, *19*, 1533–1543. [CrossRef]
95. Helman, D.; Lensky, I.M.; Tessler, N.; Osem, Y.; Helmer, E.H.; Atzberger, C.; Thenkabail, P.S. A Phenology-Based Method for Monitoring Woody and Herbaceous Vegetation in Mediterranean Forests from NDVI Time Series. *Remote Sens.* **2015**, *7*, 12314–12335. [CrossRef]
96. Sagris, V.; Dittmann, C.; Devos, W. Towards the core conceptual LPIS model. In *Proceedings of the JRC LPIS Workshop—LPIS Database Quality Assessment and Updating*; JRC: Ispra, Italy, 2007.
97. Cilek, A.; Berberoglu, S.; Kirkby, M.; Irvine, B.; Donmez, C.; Erdogan, M.A. Erosion modelling in a Mediterranean Subcatchment under climate change scenarios using Pan-European Soil Erosion Risk Assessment (PESERA). *Int. Arch. Photogramm. Remote Sens. Spat. Inf. Sci. -ISPRS Arch.* **2015**, *40*, 359–365. [CrossRef]
98. Djuma, H.; Bruggeman, A.; Camera, C.; Zoumides, C. Combining Qualitative and Quantitative Methods for Soil Erosion Assessments: An Application in a Sloping Mediterranean Watershed, Cyprus. *Land Degrad. Dev.* **2017**, *28*, 243–254. [CrossRef]
99. Kouli, M.; Soupios, P.; Vallianatos, F. Soil erosion prediction using the Revised Universal Soil Loss Equation (RUSLE) in a GIS framework, Chania, Northwestern Crete, Greece. *Environ. Geol.* **2009**, *57*, 483–497. [CrossRef]
100. Brini, I.; Alexakis, D.D.; Kalaitzidis, C. Linking Soil Erosion Modeling to Landscape Patterns and Geomorphometry: An Application in Crete, Greece. *Appl. Sci.* **2021**, *11*, 5684. [CrossRef]
101. Hooke, J.; Souza, J.; Marchamalo, M. Evaluation of connectivity indices applied to a Mediterranean agricultural catchment. *Catena* **2021**, *207*, 105713. [CrossRef]
102. Surian, N.; Righini, M.; Lucía, A.; Nardi, L.; Amponsah, W.; Benvenuti, M.; Borga, M.; Cavalli, M.; Comiti, F.; Marchi, L.; et al. Channel response to extreme floods: Insights on controlling factors from six mountain rivers in northern Apennines, Italy. *Geomorphology* **2016**, *272*, 78–91. [CrossRef]
103. Vigiak, O.; Newham, L.; Whitford, J.; Melland, A.; Borselli, L. Comparison of landscape approaches to define spatial patterns of hillslope-scale sediment delivery ratio. In Proceedings of the 18th World IMACS Congress and International Congress on Modelling and Simulation (MODSIM09), Cairns, Australia, 13–17 July 2009; pp. 3123–3129.
104. Sedighi, F.; Khaledi Darvishan, A.; Zare, M.R.; Sedighi, F.; Khaledi Darvishan, A.; Zare, M.R. Effect of watershed geomorphological characteristics on sediment redistribution. *Geomo* **2021**, *375*, 107559. [CrossRef]
105. Vanoni, V.A. Sedimentation Engineering. *Am. Soc. Civ. Eng.* **2006**, 1–418. [CrossRef]
106. Maner, S.B. *Factors Influencing Sediment Delivery Ratios in the Blackland Prairie Land Resource Area*; U.S. Department of Agriculture: Washington, DC, USA, 1962.
107. Renfro, W.G. Use of erosion equation and sediment delivery ratios for predicting sediment yield. In *Present and Prospective Tecnology for Predicting Sediment Yields and Sources*; U.S. Department of Agriculture: Washington, DC, USA, 1975; Volume ARS-S-40, pp. 33–45.
108. USDA. Sediment Sources, Yields, and Delivery Ratios. In *National Engineering Handbook*; US Soil Conservation Service: Washington, DC, USA, 1975.
109. Lagouvardos, K.; Karagiannidis, A.; Dafis, S.; Kalimeris, A.; Kotroni, V. Ianos—A Hurricane in the Mediterranean. *Bull. Am. Meteorol. Soc.* **2022**, *103*, E1621–E1636. [CrossRef]
110. Morgan, R.P.C. A simple approach to soil loss prediction: A revised Morgan-Morgan-Finney model. *Catena* **2001**, *44*, 305–322. [CrossRef]
111. Morgan, R.P.C.; Duzant, J.H. Modified MMF (Morgan–Morgan–Finney) model for evaluating effects of crops and vegetation cover on soil erosion. *Earth Surf. Process. Landf.* **2008**, *33*, 90–106. [CrossRef]
112. Collins, A.L.; Walling, D.E.; Sichingabula, H.M.; Leeks, G.J.L. Using 137Cs measurements to quantify soil erosion and redistribution rates for areas under different land use in the Upper Kaleya River basin, southern Zambia. *Geoderma* **2001**, *104*, 299–323. [CrossRef]

113. Eltner, A.; Schneider, D. Analysis of Different Methods for 3D Reconstruction of Natural Surfaces from Parallel-Axes UAV Images. *Photogramm. Rec.* **2015**, *30*, 279–299. [CrossRef]
114. Thamm, H.P.; Judex, M. The 'Low-Cost Drone'—An Interesting Tool for Process Monitoring in a High Spatial and Temporal Resolution. In *Proceedings of the ISPRS Commission VII Mid-Term Symposium 'Remote Sensing from Pixels to Processes'*; ISPRS Archives: Enschede, The Netherlands, 2006; pp. 140–144.
115. Wang, R.; Sun, H.; Yang, J.; Zhang, S.; Fu, H.; Wang, N.; Liu, Q.; Wang, R.; Sun, H.; Yang, J.; et al. Quantitative Evaluation of Gully Erosion Using Multitemporal UAV Data in the Southern Black Soil Region of Northeast China: A Case Study. *Remote Sens.* **2022**, *14*, 1479. [CrossRef]
116. Turner, D.; Lucieer, A.; Watson, C. An Automated Technique for Generating Georectified Mosaics from Ultra-High Resolution Unmanned Aerial Vehicle (UAV) Imagery, Based on Structure from Motion (SfM) Point Clouds. *Remote Sens.* **2012**, *4*, 1392–1410. [CrossRef]
117. Andaru, R.; Cahyono, B.K.; Riyadi, G.; Istarno; Djurdjani; Ramadhan, G.R.; Tuntas, S. The combination of terrestrial LiDAR and UAV photogrammetry for interactive architectural heritage visualization using unity 3D game engine. *Int. Arch. Photogramm. Remote Sens. Spat. Inf. Sci.* **2019**, *XLII-2-W17*, 39–44. [CrossRef]
118. Stumpf, A.; Malet, J.P.; Kerle, N.; Niethammer, U.; Rothmund, S. Image-based mapping of surface fissures for the investigation of landslide dynamics. *Geomorphology* **2013**, *186*, 12–27. [CrossRef]
119. Cao, L.; Liu, H.; Fu, X.; Zhang, Z.; Shen, X.; Ruan, H. Comparison of UAV LiDAR and Digital Aerial Photogrammetry Point Clouds for Estimating Forest Structural Attributes in Subtropical Planted Forests. *Forests* **2019**, *10*, 145. [CrossRef]
120. Kowalski, A.; Wajs, J.; Kasza, D. Monitoring of anthropogenic landslide activity with combined UAV and lidar-derived dems —A case study of the czerwony wąwóz landslide (SW Poland, western sudetes). *Acta Geodyn. Geomater.* **2018**, *15*, 117–129. [CrossRef]
121. Ulvi, A. The effect of the distribution and numbers of ground control points on the precision of producing orthophoto maps with an unmanned aerial vehicle. *J. Asian Archit. Build. Eng.* **2021**, *20*, 806–817. [CrossRef]
122. Yang, J.; Li, X.; Luo, L.; Zhao, L.; Wei, J.; Ma, T. New Supplementary Photography Methods after the Anomalous of Ground Control Points in UAV Structure-from-Motion Photogrammetry. *Drones* **2022**, *6*, 105. [CrossRef]
123. Waltner, I.; Saeidi, S.; Grósz, J.; Centeri, C.; Laborczi, A.; Pásztor, L. Spatial Assessment of the Effects of Land Cover Change on Soil Erosion in Hungary from 1990 to 2018. *ISPRS Int. J. Geo-Inf.* **2020**, *9*, 667. [CrossRef]
124. Yassoglou, N.J.; Kosmas, C. Desertification in the Mediterranean Europe. A case in Greece. *Communities* **2000**, 27–33.
125. Kosmas, C.; Danalatos, N.; Cammeraat, L.H.; Chabart, M.; Diamantopoulos, J.; Farand, R.; Gutierrez, L.; Jacob, A.; Marques, H.; Martinez-Fernandez, J.; et al. The effect of land use on runoff and soil erosion rates under Mediterranean conditions. *Catena* **1997**, *29*, 45–59. [CrossRef]
126. Stefanidis, S.; Alexandridis, V.; Ghosal, K. Assessment of Water-Induced Soil Erosion as a Threat to Natura 2000 Protected Areas in Crete Island, Greece. *Sustainability* **2022**, *14*, 2738. [CrossRef]
127. de Vente, J.; Poesen, J.; Verstraeten, G.; Van Rompaey, A.; Govers, G. Spatially distributed modelling of soil erosion and sediment yield at regional scales in Spain. *Glob. Planet. Change* **2008**, *60*, 393–415. [CrossRef]
128. Cerdan, O.; Govers, G.; Le Bissonnais, Y.; Van Oost, K.; Poesen, J.; Saby, N.; Gobin, A.; Vacca, A.; Quinton, J.; Auerswald, K.; et al. Rates and spatial variations of soil erosion in Europe: A study based on erosion plot data. *Geomorphology* **2010**, *122*, 167–177. [CrossRef]
129. Borrelli, P.; Märker, M.; Panagos, P.; Schütt, B. Modeling soil erosion and river sediment yield for an intermountain drainage basin of the Central Apennines, Italy. *Catena* **2014**, *114*, 45–58. [CrossRef]
130. Baggaley, N.; Potts, J. Sensitivity of the PESERA soil erosion model to terrain and soil inputs. *Geoderma Reg.* **2017**, *11*, 104–112. [CrossRef]
131. Panagos, P.; Meusburger, K.; Ballabio, C.; Borrelli, P.; Alewell, C. Soil erodibility in Europe: A high-resolution dataset based on LUCAS. *Sci. Total Environ.* **2014**, *479–480*, 189–200. [CrossRef]
132. Boomer, K.B.; Weller, D.E.; Jordan, T.E. Empirical Models Based on the Universal Soil Loss Equation Fail to Predict Sediment Discharges from Chesapeake Bay Catchments. *J. Environ. Qual.* **2008**, *37*, 79–89. [CrossRef]
133. Diodato, N.; Grauso, S. An improved correlation model for sediment delivery ratio assessment. *Environ. Earth Sci.* **2009**, *59*, 223–231. [CrossRef]
134. Lenhart, T.; Van Rompaey, A.; Steegen, A.; Fohrer, N.; Frede, H.G.; Govers, G. Considering spatial distribution and deposition of sediment in lumped and semi-distributed models. *Hydrol. Process.* **2005**, *19*, 785–794. [CrossRef]
135. Cerdà, A.; Bagarello, V.; Ferro, V.; Estaban, M.; Borja, L.; Francisco, J.; Murillo, M.; González Camarena, R. The scale effect on soil erosion. A plot approach to understand connectivity on slopes under cultivation at variable plot sizes and under Mediterranean climatic conditions. *Geophys. Res. Abstr.* **2017**, *19*, 2017–18042. [CrossRef]
136. Williams, J.R. Sediment delivery ratios determiner with sediment and runoff models. *Int. Assoc. Hydrol. Sci. Publ.* **1977**, *122*, 168–179.
137. Sloff, C.J. Reservoir sedimentation; a literature survey. In *Communications on Hydraulic and Geotechnical Engineering, No. 1991-02*; TU Delft: Delft, The Netherlands, 1991.
138. Schleiss, A.J.; Franca, M.J.; Juez, C.; De Cesare, G. Reservoir sedimentation. *J. Hydraul. Res.* **2016**, *54*, 595–614. [CrossRef]

139. Lagouvardos, K.; Kotroni, V.; Bezes, A.; Koletsis, I.; Kopania, T.; Lykoudis, S.; Mazarakis, N.; Papagiannaki, K.; Vougioukas, S. The automatic weather stations NOANN network of the National Observatory of Athens: Operation and database. *Geosci. Data J.* **2017**, *4*, 4–16. [CrossRef]
140. Le Bissonnais, Y.; Daroussin, J.J.; Jamagne, M.; Lambert, J.J.; Le Bas, C.; King, D.D.; Cerdan, O.; Léonard, J.J.; Bresson, L.M.; Jones, R.J.A. Pan-European soil crustingand erodibility assessment from the European soil geographicaldatabase using pedotransfer rules. *Adv. Environ. Monit. Model.* **2005**, *2*, 1–15.
141. Richards, L.A. The Usefulness of Capillary Potential to Soil-Moisture and Plant Investigators. *J. Agric. Res.* **1928**, *37*, 719–742.
142. da Silva, A.P.; Kay, B.D.; Perfect, E.; da Silva, A.; Kay, B. Characterization of the Least Limiting Water Range of Soils. *Soil Sci. Soc. Am. J.* **1994**, *58*, 1775–1781. [CrossRef]
143. Rabot, E.; Wiesmeier, M.; Schlüter, S.; Vogel, H.J. Soil structure as an indicator of soil functions: A review. *Geoderma* **2018**, *314*, 122–137. [CrossRef]
144. Beven, K.; Kirkby, M.; Freer, J.E.; Lamb, R. A history of TOPMODEL. *Hydrol. Earth Syst. Sci.* **2021**, *25*, 527–549. [CrossRef]
145. Beven, K.J.; Kirkby, M.J. A physically based, variable contributing area model of basin hydrology/Un modèle à base physique de zone d'appel variable de l'hydrologie du bassin versant. *Hydrol. Sci. J.* **2009**, *24*, 43–69. [CrossRef]
146. Zotarelli, L.; Dukes, M.D.; Romero, C.C.; Migliaccio, K.W.; Morgan, K.T. *Step by Step Calculation of the Penman-Monteith Evapotranspiration (FAO-56 Method)*; Institute of Food and Agricultural Sciences, University of Florida: Gainesville, FL, USA, 2013.
147. Wischmeier, W.H. A Rainfall Erosion Index for a Universal Soil-Loss Equation. *Soil Sci. Soc. Am. J.* **1959**, *23*, 246–249. [CrossRef]
148. RIST—Rainfall Intensity Summarization Tool: USDA ARS. Available online: https://www.ars.usda.gov/southeast-area/oxford-ms/national-sedimentation-laboratory/watershed-physical-processes-research/research/rist/rist-rainfall-intensity-summarization-tool/ (accessed on 28 December 2022).
149. Lykoudi, E.; Zarris, D. Identification of regions with high risk of soil erosion in the island of Cephalonia using the Universal Soil Loss Equation. In Proceedings of the Sixth National Conference of the Geographical Society of Greece, Thessaloniki, Greece, 3–6 October 2002; pp. 412–419.
150. Desmet, P.J.J.; Govers, G. A GIS Procedure for Automatically Calculating the USLE LS Factor on Topographically Complex Landscape Units. *J. Soil Water Conserv.* **1996**, *51*, 427–433.